PREPARATION OF CATALYST COATED MEMBRANES USING SCREEN PRINTING

Submitted in partial fulfillment of the requirements for the degree of
Master of Science in Engineering

Matthew Raymond Hill

I know the meaning of plagiarism and declare that all the work in the document, save for that which is properly acknowledged, is my own

Centre for Catalysis Research

Department of Chemical Engineering

University of Cape Town

Synopsis

Of the various types of fuel cells, Polymer Electrolyte Fuel Cells (PEFCs) have already been demonstrated in transportation appliances from light-duty vehicles to buses and in portable appliances including laptops and cell phones. A key component of a PEFC is its platinum electrocatalyst. With an estimated 75% of the world's platinum reserves and resources in South Africa, local development of this technology will allow South Africa to become a major player in the growing hydrogen economy. This project therefore forms part of the Department of Science and Technologies strategy, to develop fuel cell technology in South Africa. More specifically, this study aims to contribute to the development of membrane electrode assembly (MEA) platform technology at the HySA/Catalysis Centre.

In order to achieve this goal, a catalyst coated membrane (CCM) fabrication procedure was implemented using a newly acquired screen printer. In this procedure, catalyst ink is forced through a mesh onto a substrate, where it can then be transferred to a membrane via decal transfer to form a CCM. Two gas diffusions layers can then be placed on either side of the CCM forming a 5-layered MEA. Characterisation techniques of the catalyst ink, CCM and 5-layered MEA were successfully implemented such that future researchers can expand on the ideas.

Catalyst inks with varying amounts of isopropanol, 1,2-propanediol and water were screened for their suitability for screen printing. In particular the catalyst ink rheology required for a smooth and even printed surface was determined for a given screen and squeegee combination. With all the established steps in pace, screen printing proved to be a fast and reliable approach for CCM fabrication with potential for future scale up and commercialisation.

The fabricated CCMs performed on a par with a commercial Ion Power CCM, but under performed in comparison to a commercial Johnson Matthey (JM) MEA. Possible reasons for this include improved materials in the JM MEA and cell conditions favouring the JM MEA.

Future projects which specifically arise from this work entail an investigation into the water management of the fuel cell environment at HySA/Catalysis, as well as a modification of the various steps in order to optimise the process and in doing so manufacture commercially viable MEAs.

Acknowledgements

I would like to thank my supervisor, Dr Olaf Conrad, for his guidance, encouragement and willingness to help throughout the project. Furthermore, I would like to thank Nabeel Hussain, for all his help inside and outside the lab. Finally, I would like to thank the remainder of the HySA/Catalysis team for coming together and dealing with some serious problems.

Financial support from the University of Cape Town and the DST-NRF HySA/Catalysis Centre of Competence is also gratefully acknowledged.

Table of Contents

List of Figures

List of Tables

List of Symbols

E	potential	Volts
ΔG	Gibbs free energy	$J.mol^{-1}$
n	number of electrons transferred	
F	Faraday constant	96458 $C.mol^{-1}$
R	universal gas constant	8.314 $J.K^{-1}mol^{-1}$
T	Temperature	K
p	Pressure	bar
i	current density	$mA.cm^{-2}$
j	flux	$mol.s^{-1}cm^{-2}$
k	reaction rate coefficient	
C	surface concentration	
k_B	Boltzmann constant	1.381 x 10^{-23} $J.K^{-1}$
h	Planck constant	6.626 x 10^{-24} J.s
α	transfer coefficient	
i_0	exchange current density	$A.cm^{-2}$
i_o^{ref}	reference exchange current density	$A.cm^{-2}$
a_c	catalyst specific area	$cm^2.mg^{-1}$
L_c	catalyst loading	$mgPt.cm^{-2}$
ɣ	pressure coefficient	
E_c	activation energy	$J.mol^{-1}$
E_r	reversible potential	Volts
η_{act}	activation losses	Volts
η_{ohm}	ohmic losses	Volts
η_{conc}	mass transfer losses	Volts
i_L	limiting current	$mA.cm^{-2}$

D	diffusion coefficient	$cm^2.s^{-1}$
Δ	diffusion distance	cm
S	stoichiometric ratio	

Glossary

PEFC	Polymer electrolyte fuel cell
MEA	Membrane electrode assembly
CCM	Catalyst coated membrane
CCS	Catalyst coated substrate
HySA	Hydrogen South Africa
GDL	Gas diffusion layer
MPL	Micro porous layer
PFSA	Perfluorosulphonic acid
PTFE	Polytetrafluoroethylene
SEM	Scanning electron microscopy
EIS	Electrochemical impedance spectroscopy
OCV	Open circuit voltage
JM	Johnson Matthey
RH	Relative humidity

1 Introduction

This report represents a detailed investigation into the development of Membrane Electrode Assembly (MEA) platform technology at HySA Catalysis. It specifically focusses on establishing a screen printing process for the fabrication of MEAs for low temperature Polymer Electrolyte Fuel Cells (PEFC).

1.1 Background

A fuel cell is a device in which the chemical energy in hydrogen can be directly converted into electrical energy via an electrochemical reaction. With the global supply of fossil fuels decreasing, the technology represents an alternate way of generating electricity, which can be integrated with renewable H_2 products.

Of the various types of fuel cells, PEFCs have already been demonstrated in transportation appliances from light-duty vehicles to buses and in portable appliances including laptops and cell phones. Two major challenges with these fuel cells at present include the cost and durability.

A key component of a PEFC is its platinum electrocatalyst. With an estimated 75% of the world's platinum reserves and resources in South Africa, local development of this technology will allow South Africa to become a major player in the growing hydrogen economy. This project therefore forms part of the Department of Science and Technologies strategy, to develop fuel cell technology in South Africa. More specifically this study aims to contribute to the development of MEA platform technology at the HySA/Catalysis Centre.

1.2 Project scope

The project focusses on the development of a screen printing method to prepare a key component of the PEFC, the membrane electrode assembly. The focus is therefore on understanding and identifying the key steps in the preparation process and deriving a reproducible procedure for future improvements.

Even though some parameter variation is performed in the study, optimisation of the developed screen printing method falls outside the scope of this project.

2 Literature Review

2.1 Basic operation and structure of a fuel cell

A fuel cell is an electrochemical cell which converts chemical energy into electricity, with the only by products being water and heat. Redox reactions occur in a fuel cell, with, by convention, the oxidation half reaction at the anode and reduction half reaction at the cathode. The anode and cathode are separated by an ion conducting electrolyte between them. Electrons are transported from the anode to the cathode through an external circuit. A fuel cell fed with hydrogen has the following typical reactions:

Anode: $2H_2(g) \rightarrow 4H^+ + 4e^-$
Cathode: $O_2(g) + 4H^+ + 4e^- \rightarrow 2H_2O(l)$
Overall: $2H_2(g) + O_2(g) \rightarrow 2H_2O(l) + \text{electricity} + \text{heat}$ Eq. 1

Various types of fuel cells exist, typically classified by the type of electrolyte. A summary of the main fuel cell types is presented below in Table 2.1.

Table 2.1: Types of Fuel Cells (adapted from Barbir, 2005)

Type of Fuel cell	Electrolyte	Operating Temperature (°C)
Alkaline Fuel Cell	Concentrated KOH	65 - 220
Polymer Electrolyte Fuel Cell	Solid Proton Conductive Polymer Membrane	60 - 80
Phosphoric Acid Fuel Cell	Concentrated Phosphoric Acid	150 - 220
Molten Carbonate Fuel Cell	Combination of Alkali Carbonates	600 - 700
Solid Oxide Fuel Cell	Solid, Nonporous Metal Oxide	800 - 1000

At present, the majority of the hydrogen used in fuel cells comes from reforming of fossil fuels (natural gas, liquefied petroleum gas (LPG) and coal). Hydrogen via water electrolysis represents a possible future option. Current research efforts to produce the electricity for water electrolysis are based on sustainable and clean methods such as solar, hydro and wind. (Kimmel, 2012).

2.1.1 Polymer electrolyte fuel cell

There are two different types of PEFCs, namely the low temperature PEFC, operating between 60 – 80 °C, and the high temperature PEFC, operating above 120 °C. PEFC have shown promise for a number of different applications in the power range from μW to MW. One such application is in the use in vehicles, where some of the advantages of this fuel cell type are particularly favourable, viz. its high power density, quick start up procedure, good response to varying loads and low operating temperatures (Mehta & Cooper, 2003).

The main component of a PEFC is the Membrane Electrode Assembly (MEA). The MEA consists of a polymer electrolyte membrane, two catalyst layers on either side of the membrane and two gas diffusion layers on the outside of the catalyst layers. The MEA is placed between flow field plates and finally current collector plates to form a single PEFC. This setup is summarised in Figure 2.1.

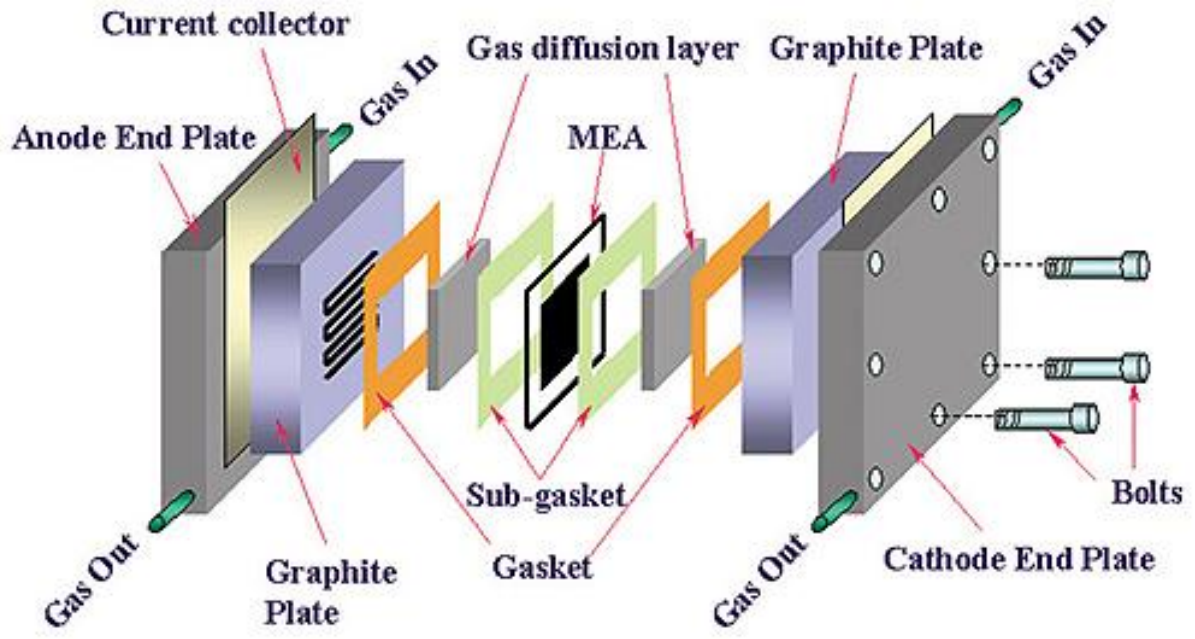

Figure 2.1: Illustration of Single PEFC (www.scientific-computing.com, 2003)

A single cell setup, as depicted in Figure 2.1, typically operates at about 600 mV with a current density of 1000 $mA.cm^{-2}$, relating to a power rating of 600 $mW.cm^{-2}$ (Hung et al., 2007). In order to obtain a higher and more useful output, cells are connected in series to create a fuel cell stack. The cells are connected via bipolar plates.

2.1.2 Fuel cell thermodynamics

The amount of heat created from the combustion of hydrogen and oxygen at 25 °C is 286 $kJ.mol^{-1}$ of hydrogen when liquid water is produced. This is known as the higher heating value of hydrogen. The lower heating value, when water vapour is produced, is 241 $kJ.mol^{-1}$. These values represent the maximum amount of energy that can be obtained from this reaction.

The portion of this energy available for electrical use corresponds to the Gibbs free energy. There are some irreversible losses in converting all the hydrogen energy into work due to the presence of entropy. The total Gibbs free energy available at 25 °C is

237 kJ.mol^{-1}. The theoretical efficiency of a fuel cell, assuming that all the Gibbs free energy can be converted into electrical energy, is therefore 83 % of the original higher heating value.

In general, the amount of electrical work is a product of the charge and the potential. In fuel cell operations the charge transferred per mole of hydrogen is the product of the electrons transferred per molecule (2 for hydrogen) and Faraday's constant. As previously mentioned the maximum electrical energy is the Gibbs free energy. The theoretical potential for a fuel cell can therefore be calculated at 1.23 V at 25 °C, with the following equation:

$$E_0 = \frac{-\Delta G_0}{nF} \quad \text{Eq. 2}$$

where for fuel cell operation the change in Gibbs free energy is expressed using the Nernst equation:

$$\Delta G = \Delta G_0 + RTln\left[\frac{P_{H_2O}}{P_{H_2}P_{O_2}{}^{0.5}}\right] \quad \text{Eq. 3}$$

2.1.3 Reaction kinetics

Reaction kinetics is the study of the rate of a chemical reaction. The rate at which the overall reaction proceeds is limited by the slowest elementary step. In fuel cell operation the limiting factor may be rate of electron transfer between the catalyst and the adsorbed substrate or the rate of adsorption or desorption of reactants. The reaction rate can therefore be easily measured by observing the current density. Faraday's Law establishes that current density i is proportional to the charge transferred:

$$i = nFj \quad \text{Eq. 4}$$

where nF (coulombs.mol^{-1}) is the charge transferred and j (mol.s^{-1}cm^{-2}) is the area specific molar reactant flux. For the case of a general redox reaction of the form:

$$Ox + ne^- \leftrightarrow Rd \quad \text{Eq. 5}$$

The flux of the forward reaction is described as:

$$j_f = k_f C_{Ox} \quad \text{Eq. 6}$$

where k_f is the rate coefficient of the forward reaction and C_{Ox} is the surface concentration of the reactant species. Similarly the flux of the reverse reaction is:

$$j_v = k_v C_{Rd} \quad \text{Eq. 7}$$

Similarly where k_v is the rate coefficient of the reverse reaction and C_{Rd} is the surface concentration of the reactant species

The net current can now be written as:

$$i = nF(k_f C_{Ox} - k_v C_{Rd}) \quad \text{Eq. 8}$$

At equilibrium, when forward and reverse reactions proceed at equal rate, the net current is zero and the rate at which each reaction is proceeding is called the exchange current density, i_0.

From the Transition State Theory (Atkins, 1998), it can be shown that the reaction rate coefficient is:

$$k = \frac{k_B T}{h} exp\left[\frac{-\Delta G}{RT}\right] \quad \text{Eq. 9}$$

where k_B is the Boltzmann constant and h is Planck constant.

For the case of the reduction half reaction, the Gibbs free energy is as follows:

$$\Delta G = \Delta G_{ch} + \alpha_{Rd} FE \quad \text{Eq. 10}$$

where "ch" refers to the chemical component and α is the transfer coefficient. Similarly for the case of the oxidation half reaction:

$$\Delta G = \Delta G_{ch} - \alpha_{Ox} FE \quad \text{Eq. 11}$$

The forward and reverse reaction rate constants can therefore be written as

$$k_f = k_{0,f} exp\left[\frac{-\alpha_{Rd} FE}{RT}\right] \quad \text{Eq. 12}$$

and

$$k_v = k_{0,v} exp\left[\frac{\alpha_{Ox} FE}{RT}\right] \quad \text{Eq. 13}$$

From Eq. 8, Eq. 12 and Eq. 13 the net current can be written as:

$$i = nF\left\{k_{0,f}C_{Ox}exp\left[\frac{-\alpha_{Rd}FE}{RT}\right] - k_{0,v}C_{Rd}exp\left[\frac{\alpha_{Ox}FE}{RT}\right]\right\} \quad \text{Eq. 14}$$

At equilibrium, the exchange current density, i_0, can be described by the following:

$$i_0 = nFk_{0,f}C_{Ox}exp\left[\frac{-\alpha_{Rd}FE_r}{RT}\right] = nFk_{0,v}C_{Rd}exp\left[\frac{\alpha_{Ox}FE_r}{RT}\right] \quad \text{Eq. 15}$$

where E_r is the reversible equilibrium potential. By combining the two equations (Eq. 14 and Eq. 15), the Butler-Volmer equation is obtained.

$$i = i_0\left\{exp\left[\frac{-\alpha_{Rd}F(E-E_r)}{RT}\right] - exp\left[\frac{\alpha_{Ox}F(E-E_r)}{RT}\right]\right\} \quad \text{Eq. 16}$$

The Butler-Volmer equation can be used to describe the net current density of an electrochemical cell operated away from equilibrium, i. e. producing or consuming electrical power. The difference between the non-equilibrium operating potential (E) and the reversible potential (E_r) is called the overpotential and it is the potential required to generate current.

At the cathode, $E < E_r$, making the first term much greater than the second term. Therefore the current at the cathode can be written as follows:

$$i = i_0 exp\left[\frac{-\alpha_{rd}F(E-E_r)}{RT}\right] \quad \text{Eq. 17}$$

Similarly for the anode:

$$i = -i_0 exp\left[\frac{\alpha_{ox}F(E-E_r)}{RT}\right] \quad \text{Eq. 18}$$

The exchange current density is a pseudo rate constant in the chemical reaction. Unlike typical rate constants, it is concentration dependent, which can be seen from Eq. 15, and is described by the following equation (Barbir, 2005):

$$i_0 = i_0^{ref} a_c L_c \left(\frac{P_r}{P_r^{ref}}\right)^{\gamma} exp\left[-\frac{E_c}{RT}\left(1 - \frac{T}{T_{ref}}\right)\right] \quad \text{Eq. 19}$$

where:

I_0^{ref} : reference exchange current density
a_c : catalyst specific area
L_c : catalyst loading
γ : pressure coefficient
T_{ref} : reference temperature, 25 °C
P_r^{ref} : reference pressure, 1 atm

P_r : reactant pressure

E_c : activation energy, 66 kJ.mol^{-1}

The exchange current density can be considered to be the readiness of the electrode to proceed with the electrochemical reaction. It is several orders of magnitude bigger on the anode side (10^{-4} vs 10^{-9} A.cm^{-2}Pt, at standard conditions), and therefore the potential-current relationship is typically modelled only by the cathode Butler-Volmer equation (Barbir, 2005).

2.2 Fuel cell components

2.2.1 Membrane electrode assembly

The MEA is the central part of a fuel cell, with the cell performance strongly linked to the optimization of this component. The three main sections, namely the polymer electrolyte membrane, catalyst layer and gas diffusion layer (GDL) are discussed in the following paragraphs and illustrated in Figure 2.2.

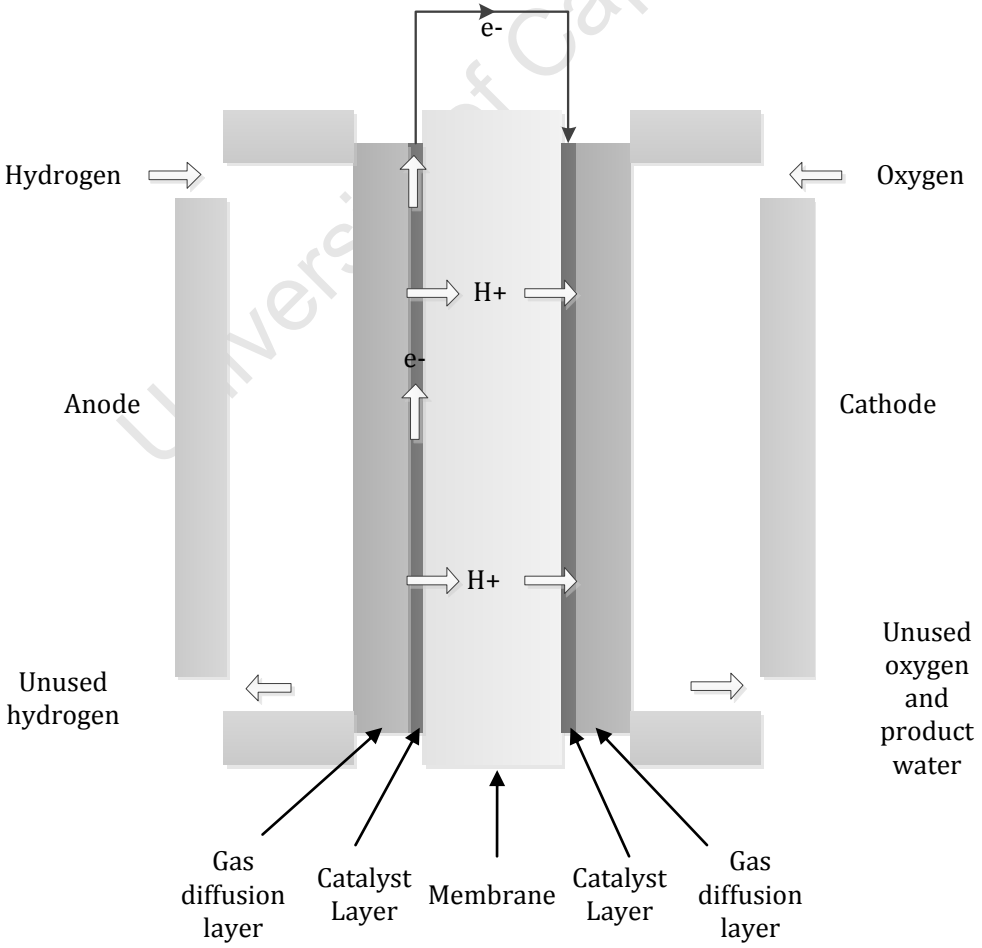

Figure 2.2: MEA schematic

2.2.2 Gas diffusion layer

The GDL is a porous and electrically conductive material on the outer ends of the MEA. The main function of the GDL is to provide a porous network in which the reactant gases can move towards the catalyst layer and the product water can move away from the catalyst layer. The GDL is therefore a porous medium with hydrophobic and hydrophilic regions in which the reactant gases and water can travel through respectively. Another function of the GDL is providing an electrical connection between the bipolar plates and the catalyst layer.

A macroporous single layered GDL structure can result in the following:

- Decreased catalyst utilisation in the MEA due to penetration of catalyst particles into the relatively large GDL pores
- Water management problems

As a result a Micro Porous Layer (MPL) is often inserted in between the catalyst layer and macro porous GDL to account for these undesirable conditions. The MPL therefore provides the following key characteristics (Han et al., 2008):

- Acts as a micro-porous support to the catalyst layer
- Minimizes electrical resistance
- Improves water management
- Prevents catalyst penetration into the macro porous GDL

A common GDL material is a carbon-fibre based porous material such as carbon paper, which is non-woven and carbon cloth. It has been shown that a mixture of the two setups (woven/non-woven) has a superior performance in comparison to carbon cloth, except at higher current densities, where the carbon cloth performs well (Stampino et al., 2009). This difference can be ascribed to the lower contact resistance between the catalyst layer and MPL. Figure 2.3 shows an example of GDLs.

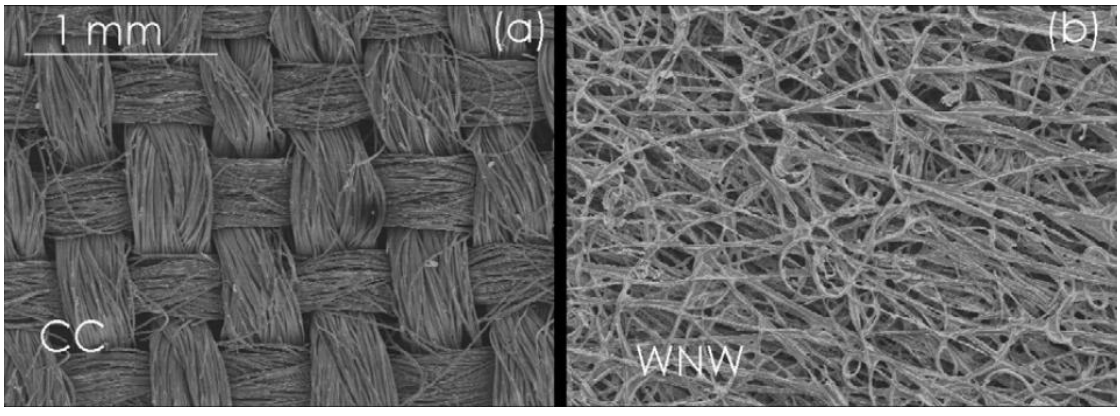

Figure 2.3: Gas diffusion layer examples (a) carbon cloth; (b) woven/non woven (Stampino et al., 2009)

2.2.3 Catalyst layer

The catalyst layer, often referred to as the electrode, is sandwiched between the membrane and the GDL. This is the reaction zone for the two fuel cell reactions. These electrochemical reactions require the presence of protons, electrons and hydrogen or oxygen, respectively, at the site of reaction. The catalyst site therefore needs to accommodate all three phases and must meet the following requirements: (Barbir, 2005)

- Electrical connection to the GDL
- Pathway for proton conduction
- Porosity, to allow reactant gases to enter and product water to leave

Figure 2.4 illustrates this so called three phase boundary condition, where the only catalyst particles being utilised are those which (i) are in direct contact with the ionomer/membrane, (ii) have an electrical connection to the GDL and (iii) are accessible by the reactants.

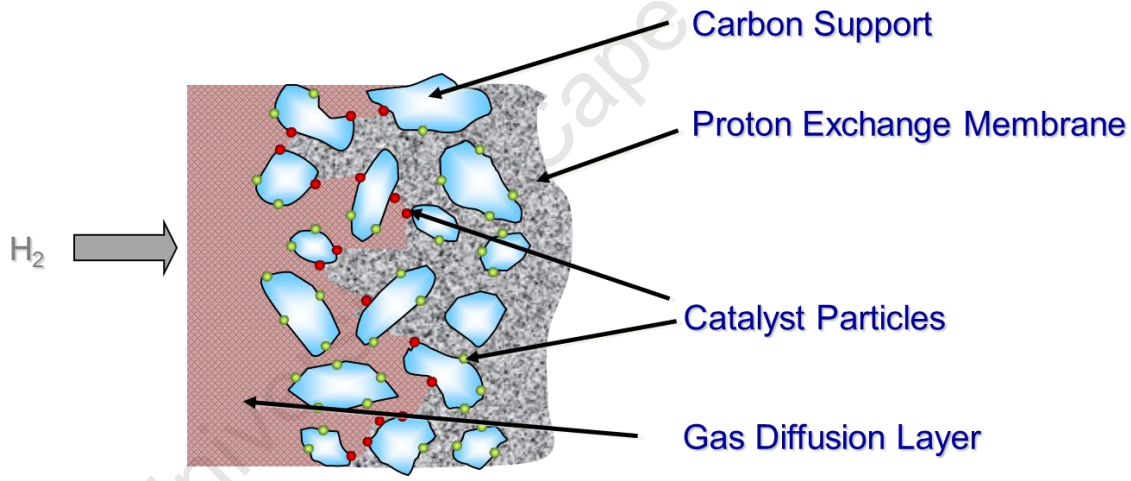

Figure 2.4: Illustration of the three phase boundary condition

The most common catalyst for both the hydrogen oxidation and oxygen reduction half reactions is platinum supported on carbon black. Typical total platinum loadings in commercially available MEAs are 0.6-0.8 $mg.cm^{-2}$. To achieve commercial viability the Pt content needs to be further reduced to approximately 0.15 mg $Pt.cm^{-2}$, whilst maintaining the same fuel cell performance (Gasteiger et al., 2005).

2.2.4 Polymer electrolyte membrane

The polymer electrolyte or proton exchange membrane allows for the transport of the protons from the anode to the cathode. Perfluorosulphonic acid (PFSA) polymer is the

most commonly used ionomer to produce membranes. This material consists of three distinct regions:

- Polytetrafluoroethylene (PTFE) acting as a backbone structure
- Ether-linked side chains of varying length and flexibility connecting the PTFE backbone to the superacidic region
- Sulphonic acid moieties that are more strongly acidic than sulphuric acid

A schematic of the PFSA structure is shown below:

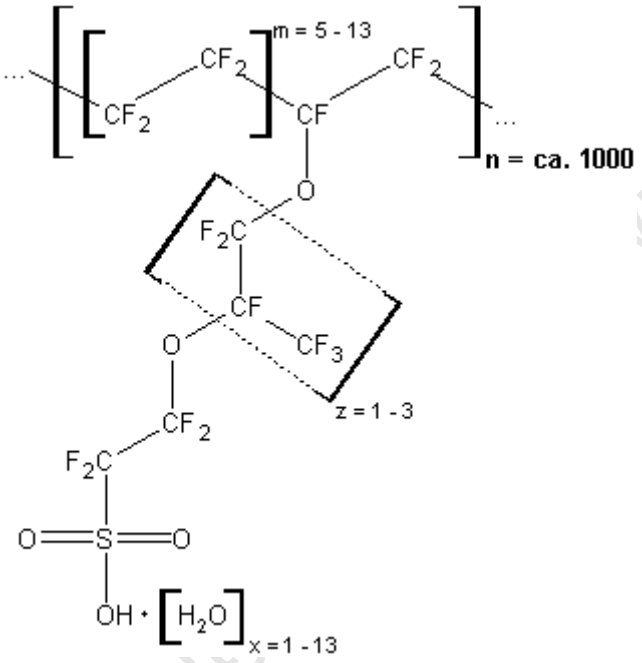

Figure 2.5: Schematic of PFSA (www.mecadi.com, 2013)

Upon hydration of the membrane, the H^+ ions from the sulphonic acid group become mobile as hydronium ions, allowing for movement between the sulphonic acid sites (Mehta & Cooper, 2003).

The major advantages of using PFSA based membranes include:

- PTFE backbone allows the membrane to be chemically active and durable at the PEFC operating conditions.
- Mobility of H^+ under good humidification conditions translates to a very low voltage drop due to ohmic resistance, approximately 50 mV at 1000 m $A.cm^{-2}$.

In order to enhance the three phase region, an ionomer is added to the catalyst layer. This is a solubilised form of the membrane and extends the proton conduction paths into the porous GDL structure, connecting more catalyst sites to the membrane. An important part of optimising catalyst utilisation and therefore MEA performance is the ionomer to carbon ratio and the ionomer solids weight percent. These two parameters are typically between 0.8 – 1 and 0.25 – 0.35 wt% respectively (Kocha, 2003).

2.2.5 Bipolar plates

Bipolar plates are placed on either side of the MEA and therefore have the following key components (Mehta & Cooper, 2003):

- Distribute reactants within a cell
- Facilitate water management
- Separate individual cells in a stack
- Carry current away from the cell
- Facilitate heat transfer from or to the stack

Bipolar plates are most commonly made from graphite, moulded graphite composite or metal.

2.2.6 Summary

This thesis focusses on the best approach for one set of materials and designs: Nafion® 212, Freudenberg GDL, graphite bipolar plates with hybrid serpentine flow field and Sainergy 40% Pt/C. The resulting MEA will therefore not be a universal technology. Rather the developed method of preparation and tools for characterisation will enable future researchers at HySA/Catalysis to find the best compromise in a different parameter set.

2.3 MEA fabrication

2.3.1 Fabrication methods

There are two major routes to prepare a MEA. In the first method, the catalyst layer is coated onto the membrane to make a catalyst coated membrane (CCM). It can then be combined with two GDLs via a hot press step. In the second method, catalyst is coated onto the GDL to form a catalyst coated substrate (CCS), two of which are then hot pressed with the membrane to form a MEA. The two routes are summarised by Figure 2.6.

Both of these methods have been successfully demonstrated on a commercial scale. Thanslip & Hunsom (2010) showed that the contact resistance between the catalyst layer and membrane was less for the CCM technique. A lower contact resistance results in improved MEA performance. However, Song et al. (2006) improved the catalyst utilisation using the CCS technique.

Literature gives many examples of both techniques being applied, examples of the CCM technique include Millington et al. (2011) Rodgers et al. (2012) and Debe (2012).

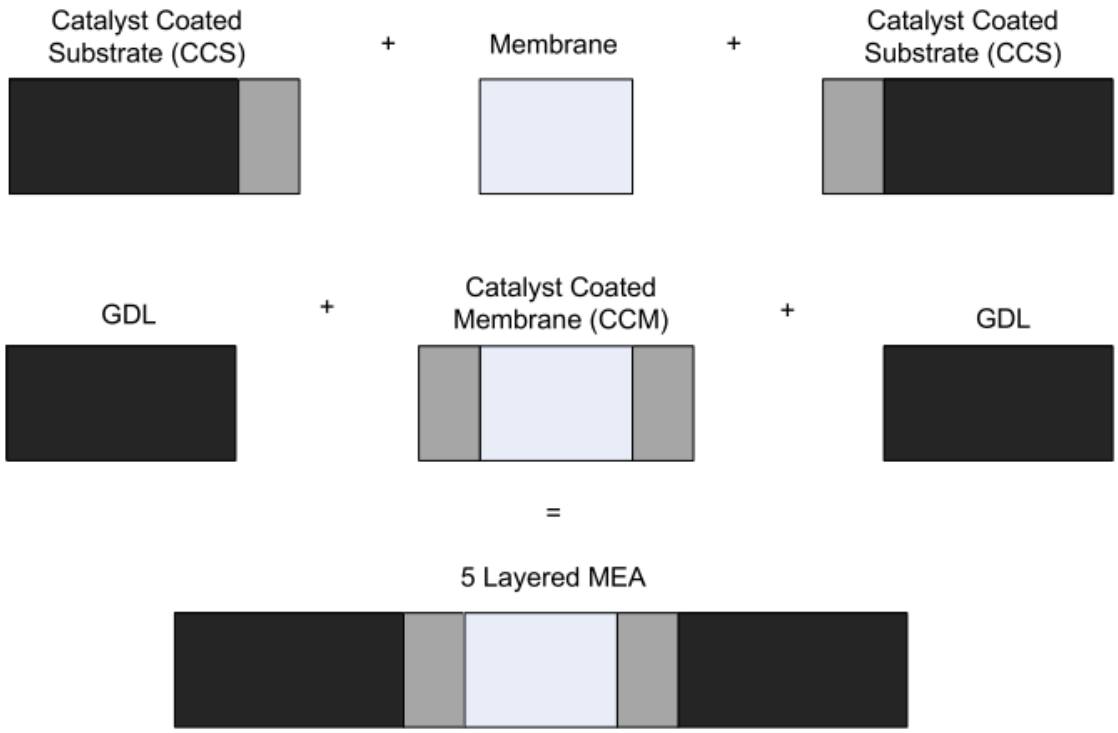

Figure 2.6: MEA fabrication methods (adapted from Kocha, 2003)

2.3.2 CCM preparation methods

The CCM can be prepared by direct coating or by coating on a substrate followed by a decal transfer.

2.3.2.1 Direct coating

In the direct coating method, the catalyst layer is coated directly onto the membrane. The major disadvantage of this method is that the membrane tends to swell during the application, leading to a poor dispersion, uneven coating or cake formation.

2.3.2.2 Decal transfer

In the decal transfer technique, the catalyst layer is coated onto a substrate (such as a sheet Teflon or polyamide) and then transferred onto the membrane after the drying process (Bender et al., 2003). The disadvantage with this method is the potential loss of active catalyst during the transfer from substrate to membrane.

2.3.3 Hot pressing

Hot pressing is the next step in the fabrication of an MEA. This method is the most common way to assemble the MEA and results in a good contact between the electrode and the membrane. The parameters in this step are temperature, pressure and time.

2.3.4 Ink deposition method

2.3.4.1 Screen printing

Screen printing is a common method of applying the catalyst ink to the membrane or substrate (Tang et al., 2007; Hobson et al., 2002). The process of screen printing entails of forcing an ink through a print matrix and depositing it on the desired surface. The print matrix consists of a mesh of wires that allows for ink to penetrate during the printing process. The free volume can be controlled by the mesh count therefore controlling the amount of ink that is transferred onto the printed surface. This process is summarised in Figure 2.7.

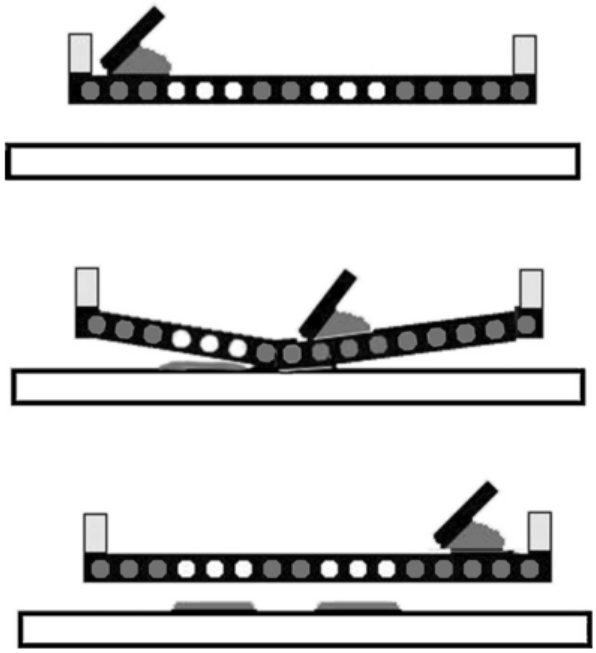

Figure 2.7: Schematic of screen printing process (Bonifacio et al., 2011)

Screen printing is a form of stencilling and was developed in China, during the Song Dynasty, between 960 – 1279 AD (Sheng, 1999). In 1907 screen printing was introduced in Europe, but it was not until after the World War II that it was used on an industrial scale. The process can be used to create many shapes and sizes, with many types of ink, giving it many uses ranging from simple t-shirt designs to highly complex printed circuit boards (Roberts, 2006).

MEA fabrication via CCS or CCM is therefore a natural choice for the application of the screen printing process. With a highly defined shape, thickness and even distribution, screen printing is a common method of catalyst ink deposition.

An important factor when considering screen printing is the flow properties of the material that is being printed. Viscosity and its change under mechanical stress are an

important aspect of the flow property. The change in viscosity during the printing process is summarised in Figure 2.8.

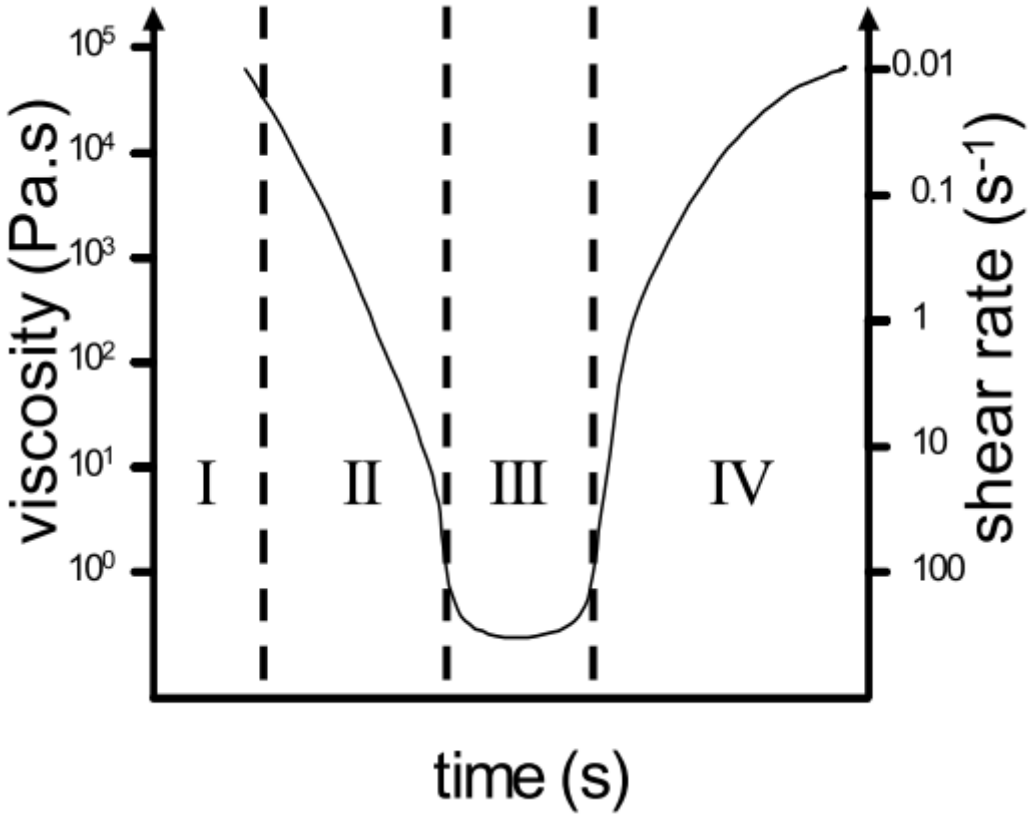

Figure 2.8: Viscosity and shear rate during screen printing (Phair & Kaiser, 2009)

Four distinct regions are seen in Figure 2.8 showing the change in the ink's viscosity during the printing process. Starting from the ink at rest with a relatively high viscosity (I), the viscosity decreases several orders of magnitude as the ink experiences mechanical shear stress when it is forced through the mesh by a squeegee (II). The point of minimum viscosity is reached as the ink exits on the opposite side of the mesh and is deposited on the substrate (III). As the mesh snaps, the ink relaxes back to its resting state at high viscosity (IV).

The shear rate during screen print can range from 0 – 1000 s^{-1}, with a typical print operating at a maximum 300 s^{-1}. Seeing as a paste is required which can flow at these high shear rates, it is important for the paste to be shear thinning to flow under high mechanical stress as well as unchanging over time such that run off does not occur in the final stage. The characterisation of the flow properties therefore allows for the optimisation of the printing process.

The flow properties of the ink must be matched to the mesh matrix and vice versa. To select the correct matrix, the free space between the wires is calculated and compared to the space needed for the catalyst ink to achieve the desired loading (Bonifacio et al., 2011).

The final aspect on MEA preparation using a screen printer is the choice of CCM or CCS. Screen printing has been successfully demonstrated for both CCS and CCM. However, in order to align the study with the goals at HySA/Catalysis, the CCM pathway was chosen in order to establish a protocol for future researchers.

The properties of the catalyst ink used to create the MEA are very important. It typically consists of the platinum on carbon support, mixed with some organic solvent and an ionomer solution. Various solvents are reported, including ethylene glycol, 1,2-propandiol and propylene glycol (Chisaka et al., 2010). The ionomer to carbon ratio and the ionomer solid weight percent in the final catalyst layer is typically between 0.8 – 1 and 0.25 – 0.35 weight percent respectively (Kocha, 2003). The concentration of ionomer solution used is depended on the required viscosity of the catalyst slurry. Screen printing requires a more viscous ink than other methods such as spraying and therefore needs less solvent in the mixture, leading to a higher ionomer concentration being used.

2.3.4.2 Other ink deposition methods

Various other methods exist for both CCM and CCS preparation. The most commonly applied methods are spraying (Tang et al., 2007) and blade coating based methods (Stampino et al., 2009). The choice of method is dependent on several factors such as scalability, reproducibility, time and eventual application. The purpose of this study is to establish a screen printing method at HySA/Catalysis to complement the existing competency in spraying and blade coating based methods.

2.4 Characterisation techniques

Various techniques can be used to characterise the catalyst ink and MEA. These techniques are discussed briefly in this section.

2.4.1 Study of rheological properties

Rheology is the study of the flow and deformation of matter as a result of stress (Giacomin, 2011). Rheological studies can therefore be fruitfully applied in the characterisation of the catalyst inks developed for a printing process. During the application process, be it blade coating, spraying or screen printing, the catalyst ink is

subject to processes inducing stresses, making the rheological properties important to consider. The rheological properties of an ink can therefore yield valuable insights into the ink behaviour during the deposition process.

These properties include the yield stress, which can be linked to how thick the coating is, thixotropy, which is the time dependence of the viscosity and the levelling off viscosity at high shear rates due to the surface tension. Typically an ink containing solids and polymers will initially decrease in viscosity at increasing shear rate, due to the ordering of the molecules, followed by a stable point, after which it will increase due to tight packing of the molecules. This is illustrated in Figure 2.9.

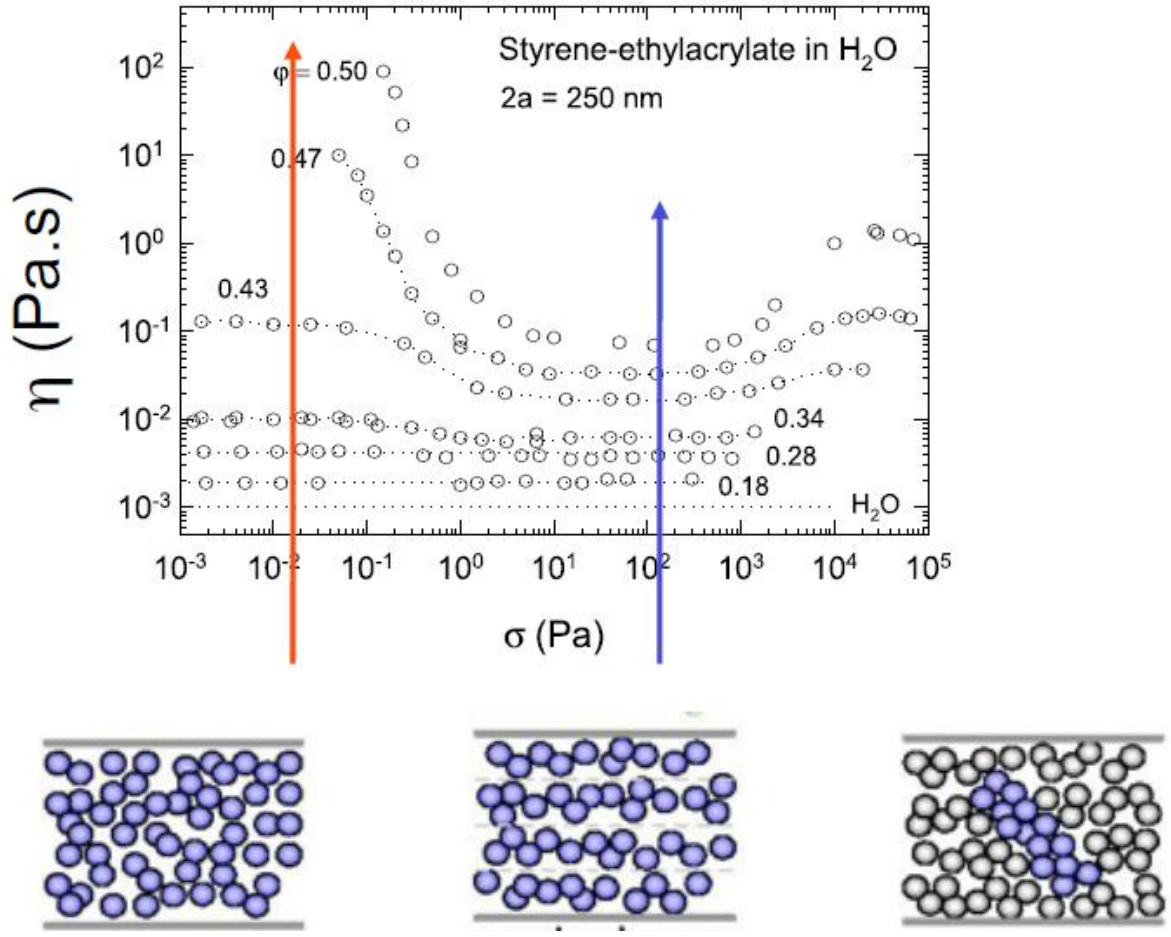

Figure 2.9: Rheological properties at increasing shear (Fuller, 2011)

Apart from the above mentioned factors, rheology controls the evenness of the of the catalyst layer. Too low viscosity at low shear rates will result in the ink running after the deposition. The rheology also plays a part in indicating the dispersion of the catalyst particles in the catalyst layer. Rheology of paints and inks is therefore an important science in the painting and printing industries.

2.4.2 Scanning electron microscopy

Scanning electron microscopy (SEM) is used to inspect the topography and, when coupled with energy dispersive spectroscopy, give elemental information of a specimen. The SEM uses an electron beam with a wavelength of 0.12 Angstroms to achieve a magnification of up to 10000x. A magnification of 10000x gives insight into the various layers of the MEA, including the effectiveness of the application and the thickness of the various layers. It therefore presents a good method to examine the surface of the catalyst layer. The data can give information on the surface cracks, catalyst layer thickness and evenness and an estimation on the particle and pore size. SEM is therefore a commonly used ex-situ MEA characterisation technique (Su et al., 2010; Ferreira et al., 2005; Millington et al., 2011).

In SEM, a beam of electrons is focussed on a specific area of the sample, creating an energy transfer at this point and generating a variety of signals that can be recorded by suitable detectors. The primary electrons dislodge secondary electrons, which are collected by a detector. To produce an image, the beam is swept across sample, thus generating a topographic image via the collection of the secondary electrons.

This process also generates backscattered electrons, primary electrons that bounce off the nuclei of atoms in the sample. These backscattered electrons possess more energy than the secondary electrons and have a defined direction and therefore require a different detector. The secondary electrons allow for good contrast of the image and provide information on the differences in atomic number in the sample. Other signals include X-ray, light, heat and transmitted electrons (Liao et al., 2008), all of which can add further investigation if a suitable detector is available.

SEM imaging can therefore provide high resolution images, quantitative elemental analysis and fast elemental mapping.

2.4.3 Polarisation curves

A polarisation curve is a very important characterisation tool for fuel cells because the operating conditions are close to that of fuel cell applications. It displays the potential difference between two terminals of a fuel cell as a function of the current passing through a variable resistive load. If a single cell is between the two terminals and the current is normalised against the electrode area, fundamental properties of the fuel cell can be quantified. The curve is used for diagnostic purposes, as well as for sizing and control. From the polarisation curve, a power curve can be easily derived. An example of a polarisation curve is shown in Figure 2.10.

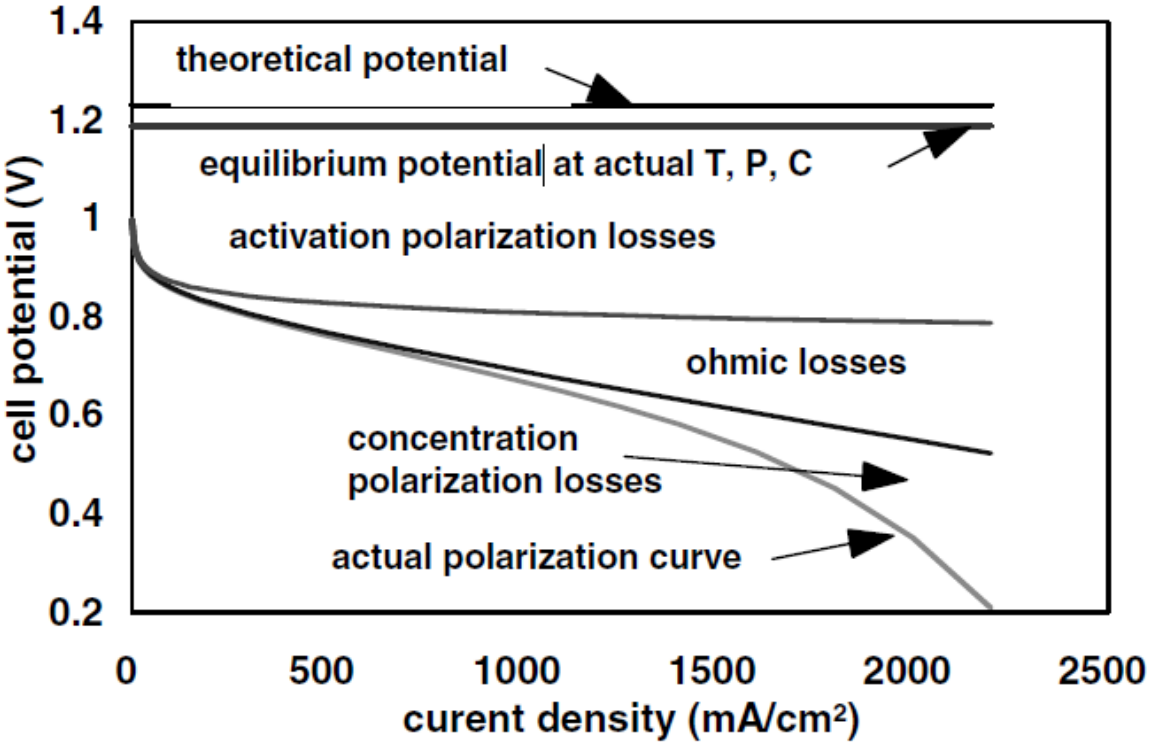

Figure 2.10: Example of polarisation curve showing losses (adapted from Barbir, 2005)

As seen in Figure 2.10, the cell voltage decreases with increasing current density. This is due to a large number of effects. Even when no current is generated (i.e. when the electric load has an extremely high (infinite) resistance), there are voltage losses due to crossover of fuel through the electrolyte, electronic conduction through the electrolyte, and oxidation of catalyst and electrode materials. The combined effects of these losses account for the difference between the theoretical potential and the actual equilibrium potential at open cell voltage (Cooper et al., 2008).

The theoretical cell potential can be described by the Nernst equation (Eq. 3) at standard conditions. Similarly, the equilibrium potential can be described by the Nernst equation at actual conditions. Activation polarisation, also known as the kinetic limitations, are associated with overcoming the activation energy in the chemical reaction and are therefore a function of temperature, pressure, concentration and electrode properties. Because the region is completely controlled by the kinetics of the reaction, one can use the Butler-Volmer and exchange current density (Eq. 15 and Eq. 16) to estimate performance.

A simplified way to show the activation losses is using the Tafel equation, which is obtained from the linearization of the Butler-Volmer equation, and can be shown as follows:

$$\eta_{act} = a + blog(i) \quad \text{Eq. 20}$$

where

$$a = -2.3\frac{RT}{\alpha F}\log(i_0) \quad \text{Eq. 21}$$

and

$$b = 2.3\frac{RT}{\alpha F} \quad \text{Eq. 22}$$

The ohmic losses seen in the performance of the fuel cell are attributed to the ionic current in the electrolyte, interfacial contact resistance and electronic current in the electrodes. The electronic current losses are however much smaller than the losses associated with ionic current losses. This loss arises from the transport of the proton through the polymer membrane and catalyst layer.

The ohmic losses in the cell can be quantified using a technique called current interrupt. In the current interrupt technique, current is interrupted from the electrochemical cell for a short time, so that the voltage drop across the non-electrode components is reduced to zero, and the measured polarization is that of the electrode itself. The cell voltage before and after interruption gives the resistance in the ohmic region, (Williams et al., 2005) and can be shown as follows:

$$\eta_{ohm} = iR \quad \text{Eq. 23}$$

A plot of potential loss log(i) of the data after correction for internal resistance yields a representation with sections nearly linear over a range of two to three decades. By using Eq. 20, parameter b, the so-called Tafel slope, and the parameter a, containing the exchange current density, i_0, can be extracted.

The final limitation observed in the polarisation curve is associated with transport losses. Transport limitations can be described by mass transfer controlling the reaction, shown by the following equation:

$$\eta_{conc} = \frac{RT}{nF}ln\left(\frac{i_L}{i_L - i}\right) \quad \text{Eq. 24}$$

where i_L is the limiting current density, and is described as the current density at which the surface concentration of reactant reaches zero, with the following equation:

$$i_L = \frac{nFDC_B}{\delta} \quad \text{Eq. 25}$$

where:

D = Diffusion coefficient
δ = Diffusion distance

Another way to characterise mass transfer limitations is to compare polarisation curves of a cell run under oxygen, helox (mixture of oxygen and helium with the percentage of oxygen as that of air) and air. Because oxygen diffusion in helium is noticeably faster than in nitrogen, the performance of the helox curve should be better than that of the air curve, but worse than that of the oxygen curve. The differences observed can be explained by the changing partial pressure of oxygen affecting both the Nernst equation (Eq. 3) and the exchange current density (Eq. 19). The cell potential loss from oxygen to air can therefore be modelled as follows:

$$\Delta V = \frac{RT}{nF}\left[\left(\frac{1}{0.21}\right)^{0.5}\right] + \frac{RT}{\alpha F} ln\left(\frac{1}{0.21}\right) \quad \text{Eq. 26}$$

Accounting for all these losses, the actual potential of a cell is therefore:

$$V_{cell} = E_{theor} - \left(\left|n_{act,c}\right| + n_{act,a}\right) - n_{ohm} - \left(n_{conc,c} + n_{conc,a}\right) \quad \text{Eq. 27}$$

where

E_{theor} = theoretical potential
n_{act} = activation losses
n_{ohm} = ohmic losses
n_{conc} = concentration polarisation losses

The power density (W.cm^{-2}) delivered from the fuel cell is the product of the current density and the voltage. It can therefore be obtained from the polarisation curve and represents a common method to describe the fuel cell performance. Other important terms to describe the fuel cell include the volumetric power density (W.cm^{-3}) and specific power density (W.kg^{-1}) (Barbir, 2005).

2.4.4 Electrochemical impedance spectroscopy

Electrochemical Impedance Spectroscopy (EIS) is a technique whereby electrochemical system is characterised by applying a sinusoidal perturbation of the voltage (potentiostatic mode) or the current (galvanostatic mode) over a range of frequencies and observing the electrical response. By introducing the frequency domain (and

therefore a time domain) over a range from mHz to MHz processes on different time scales from instantaneously to minutes can be decoupled.

One convenient method to analyse EIS data is by interpreting the frequency response through an equivalent circuit model. This model represents the dominant electrochemical and fluid dynamic factors in combinations of capacitors, inductors and resistors. EIS is therefore mainly an in-situ technique to diagnose fuel cell properties and performance (Yaun et al., 2010).

Fuel cells are most commonly modelled using the Randle's equivalent circuit (Figure 2.11).

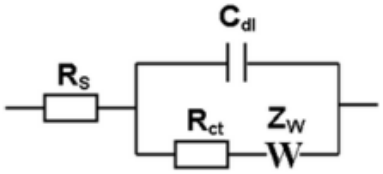

Figure 2.11: Randles Equivalent Circuit

The following key parameters are modelled in the equivalent circuit and fitted to the experimental data:

R_s: Uncompensated solution (ohmic) resistance
R_{ct}: Charge transfer resistance
Z_w: Warburg impedance or mass transfer resistance
C_{dl}: Double layer capacitance

Electronic components are used to model physical phenomena in the electrochemical system in response to an electrochemical stimulus. They are charge-transfer resistance, contact resistance, oxidant and fuel transport resistance, water transport resistance and proton transport resistance. The charge-transfer resistance is the resistance that occurs when electrons transfer across the electrolyte. The electronic resistance (wires, conducting polymers, etc) is typically ignored because it is very small in comparison with the proton transport resistance.

If a layer of non-conductive medium is in between two electrodes and an electrical current passes through it, charge is stored at both electrodes, called a capacitor. The contributor to capacitance is the double-layer capacitance. In typical fuel cell testing, true double layer capacitance does not exist. The behaviour of the capacitance is modelled by the constant phase element and with a factor n, where $0<n<1$. The more the constant phase element behaves like the double layer capacitance, the closer n will be to 1.

The resulting data obtained from EIS offers several advantages as a characterisation technique. The main advantage of EIS is that it serves as a diagnostic tool to identify individual contributors to the circuit in a short period of time, potentially isolating problem areas.

Numerical values can be found for these terms by least-squares fits of the corresponding values of suitable equivalent circuits to the observed spectra such as in Figure 2.12.

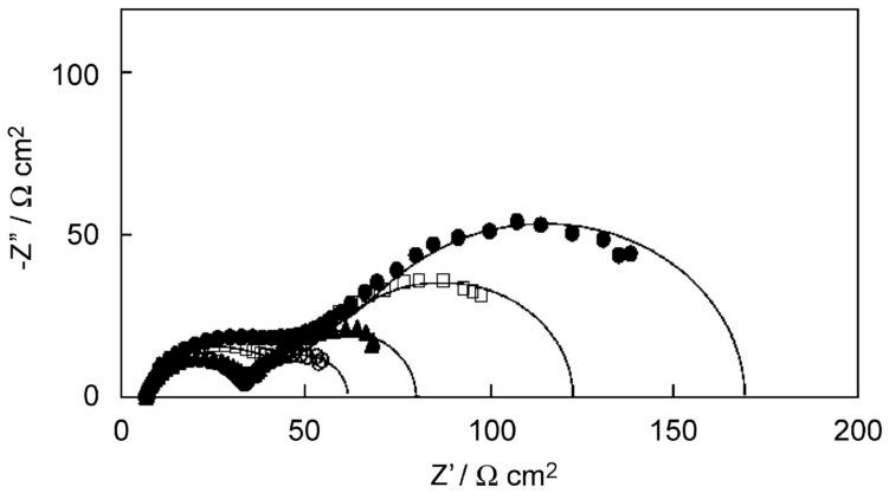

Figure 2.12: Example of EIS representation in a Nyquist plot (Yaun et al., 2007)

Two semi-circles are observed in Figure 2.12, the smaller semi-circle on the left is due to the resistance in the anode and the larger semi-circle is due to the presence of the cathode. Typically the resistance in the cathode is so much larger than the anode, that only the semi-circle for the cathode is observed.

EIS therefore represents a powerful and frequently used tool for the characterisation of an MEA. (Yaun et al., 2007; Frey & Linardi, 2004; Su et al., 2010).

2.5 Water management

When fully humidified, the polymer electrolyte membrane becomes an excellent protonic conductor. Water management in a fuel cell ensures that the membrane remains fully hydrated to maintain this good ionic conductivity and performance.

The water content of the membrane is determined by the balance between water production and three water transport processes, which include electro-osmotic drag of water, associated with the proton migration through the membrane from the anode to the cathode; back diffusion of product water from the cathode; and transport (evaporation and condensation) of water to and from the reactant gas streams. This

water balance is shown schematically in Figure 2.13. Without control of these factors, a difference between production and removal rates of water can occur (Berning & Djilali, 2003).

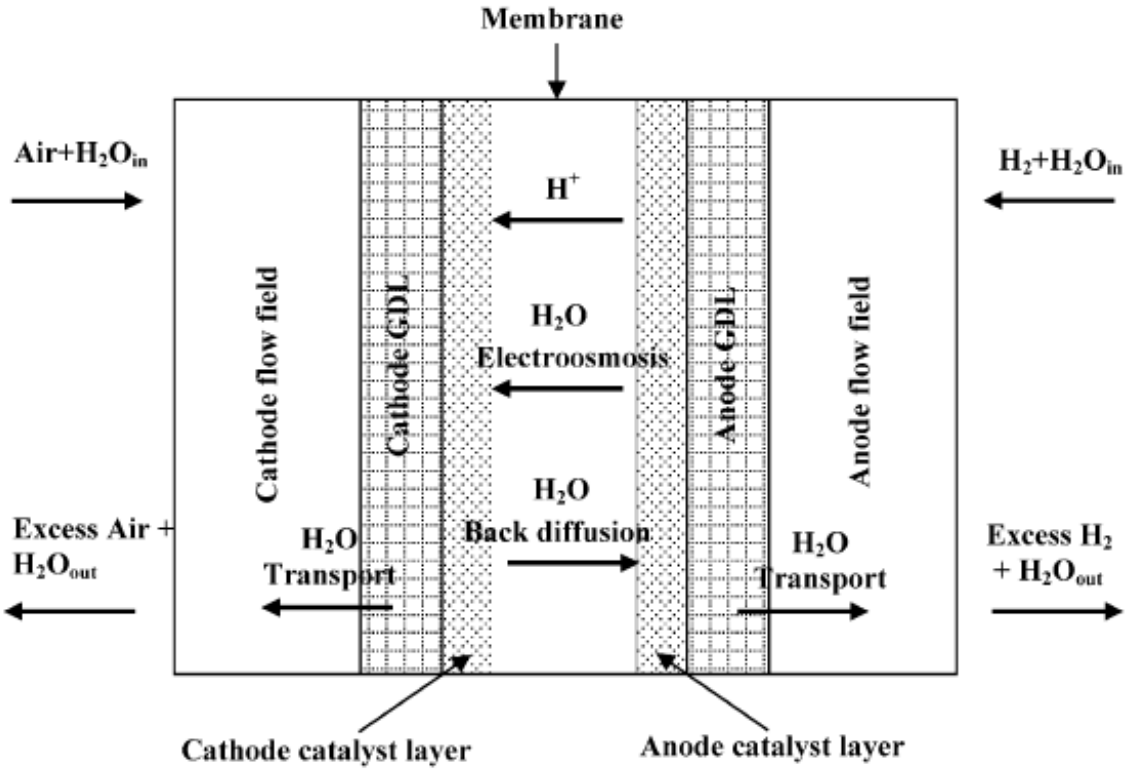

Figure 2.13: Water movement inside a PEFC (Li et al., 2008)

An excess of water in catalyst layer, GDL or flow channels is called flooding and results in a loss of performance due to difficulty of reactant gases reaching the catalyst sites. Too little water causes the ionomer content of the electrode and the membrane to dry out, resulting in an increase in the cell resistance and therefore decreasing performance (Barbir, 2005).

The polarisation curve measurement is typically carried out by incrementally increasing the current drawn from the cell and recording the cell voltage. The flow rate of reactant gases is increased as the current is increased at constant stoichiometry. Once a low operating voltage has been reached (typically 0.45V) the current is then incrementally decreased back to 0. If the 'up' and 'down' curves of a single MEA at specific conditions show a hysteresis, it is possible that there is either flooding or drying in the cell.

Flooding typically occurs at high current densities where excess water is formed. This leads to mass transfer issues which hinder the performance. Drying is more common at lower current densities.

2.6 Performance of MEAs in literature

Table 2.2: Performance of MEAs at 0.6 V

Method	CCM or CCS	Catalyst Loading (mg Pt.cm^{-2})	Operating conditions	Current densities at 0.6 V (mA.cm^{-2})	Source
Spraying	CCS	0.15	Oxygen, 60 °C, 1 bar	200	(Thanslip & Hunsom, 2010)
Spraying	CCM	0.15	Oxygen, 60 °C, 1 bar	300	(Thanslip & Hunsom, 2010)
Spraying	CCM – decal	0.15	Oxygen, 60 °C, 1 bar	350	(Thanslip & Hunsom, 2010)
Spraying	CCM – decal	0.2	Oxygen, ambient temperature, 1 bar	930	(Tang et al., 2007)
Screen Printing	CCS	0.2	Oxygen, ambient temperature, 1 bar	900	(Tang et al., 2007)
Screen Printing	CCS	0.6	Oxygen, 75 °C, 1 bar	800	(Bonifacio et al., 2011)
Screen Printing	CCM – decal	0.4	Air, 60 °C, 1 bar	470	(Rajalakshmi & Dhathathreyan, 2007)
Screen Printing	CCS	0.3	Oxygen, 70 °, 1 bar	850	(Hwang et al., 2011)

Table 2.2 shows the performance of various MEAs at 0.6 V and at varying catalyst loadings, feed gases, temperatures, pressures and relative humidities. 0.6 V was chosen as a comparison point as this represents a typical operating voltage in several fuel cell applications. Since operating conditions varied significantly between the different MEAs, a direct comparison between all the MEAs is not correct. One therefore needs to be very careful when drawing conclusions based on the literature data.

However, for instances where operating conditions were the same, the CCM decal was observed to be a superior technique to CCM direct spray or CCS (Thanslip & Hunsom, 2010). Furthermore the table shows that screen printing has been successfully used to prepare both CCM and CCS (Hwang et al., 2011; Rajalakshmi & Dhathathreyan, 2007).

3 Objectives

A short term goal at the HySA/Catalysis Competence Centre is the establishment of platform technology for fuel cell catalytic devices such as the membrane electrode assembly (MEA). To achieve this, an understanding and competency in state-of-art lab scale MEA fabrication techniques is required. Based on the above literature, screen printing has shown promise as a method of producing MEAs with state-of-art performance. In particular, it is an attractive method for preparing catalyst coated membranes via decal transfer.

The primary objective of this study is to develop and establish a reproducible lab scale procedure for the fabrication of MEAs using screen printing. The CCM technique is applied in order to align the project with HySA/Catalyst goals. In the process establishing the method, an understanding of the key parameters affecting the screen printing procedure, namely the catalyst ink rheology and the printing operating parameters will be developed.

In order to evaluate the quality of the screen printing coatings, ex-situ techniques prior to fuel cell testing are required. The project therefore also aims to implement and establish well known techniques for ex-situ characterisation of the catalyst layer coatings, which up to this stage had not been implemented at HySA/Catalysis. This includes rheological studies of the catalyst ink, and SEM imaging of the catalyst layer on the membrane.

Further in-situ techniques, polarisation curves and EIS, are required to characterise the successfulness of the MEA fabrication. MEA comparison will be conducted by testing commercial MEAs at HySA/Catalysis.

Specifically, this study seeks to investigate the following:

1. The effect of the ink rheology on the screen printing process
2. Establish a set of screen printing parameters
3. In-situ reproducibility of CCM preparation procedure
4. In-situ fuel cell performance of various CCM-GDL combinations

4 Experimental

This section details the experimental procedure for the preparation of the catalyst coated membranes via the screen printing technique and the testing of the resultant MEA in a fuel cell environment.

4.1 Preparation of catalyst coated membranes

CCM's were prepared using a decal transfer technique where the catalyst ink is first coated onto a substrate and subsequently transferred onto both sides of a membrane. All the MEA components were commercially sourced.

4.1.1 Description of MEA components

Table 4.1 summarises the components used during the CCM and MEA fabrication process.

Table 4.1: MEA components

Component	Manufacturer	Description	Code
Catalyst	Sainergy	Pt/C, 40 wt%	XC 72
GDL	Freudenberg FCCT	Carbon paper with MPL	H2315 C1
	Toray	Carbon paper with MPL	060T
	Sigracet	Carbon paper with MPL	24 BC
Membrane	Du Pont	Nafion® 212	
Decal substrate	Du Pont	Kapton 125 micron	500 HN
Nafion® solution	Ion power	15 wt% solution (1100 EW)	

4.1.2 Catalyst ink formulation and preparation

Catalyst ink consisted of Pt/C catalyst, ionomer solution, organic solvent (mixture of 1,2-propanediol and isopropanol) and de-ionized water. The ionomer content and the ionomer:carbon ratio of the ink were 32% and 0.8:1 respectively.

The catalyst ink was prepared in three major steps:

Step 1: De-ionised was slowly added dropwise (500 µL per drop) to 1 g of catalyst in a 20 ml glass vial. Care was taken to wet the whole catalyst surface prior to the addition of organic solvent. The organic solvent consisted of 1,2-propanediol and isopropanol and was varied from experiment to experiment. This mixture was placed on a Heidodlph MR Hei-End magnetic stirrer at 50 rpm.

Step 2: 2.8 mL of ionomer was then added dropwise to the stirring mixture. The mixture was then sealed and stirred for 30 min at 300 rpm.

Step 3: The catalyst ink was finally ultrasonicated in a Grant ultrasonic bath at room temperature for 30 min. The ink was then immediately used for screen printing.

4.1.3 Application of catalyst ink

The catalyst ink was applied onto the Kapton® substrate using the screen printing technique. The screen printer used was from Systematic Automation Inc, model 810-30. It has the option to change the speed, pressure and angle of the squeegee. Squeegee and printing screens were obtained from Color Screen. The screen is depicted in Figure 4.1:

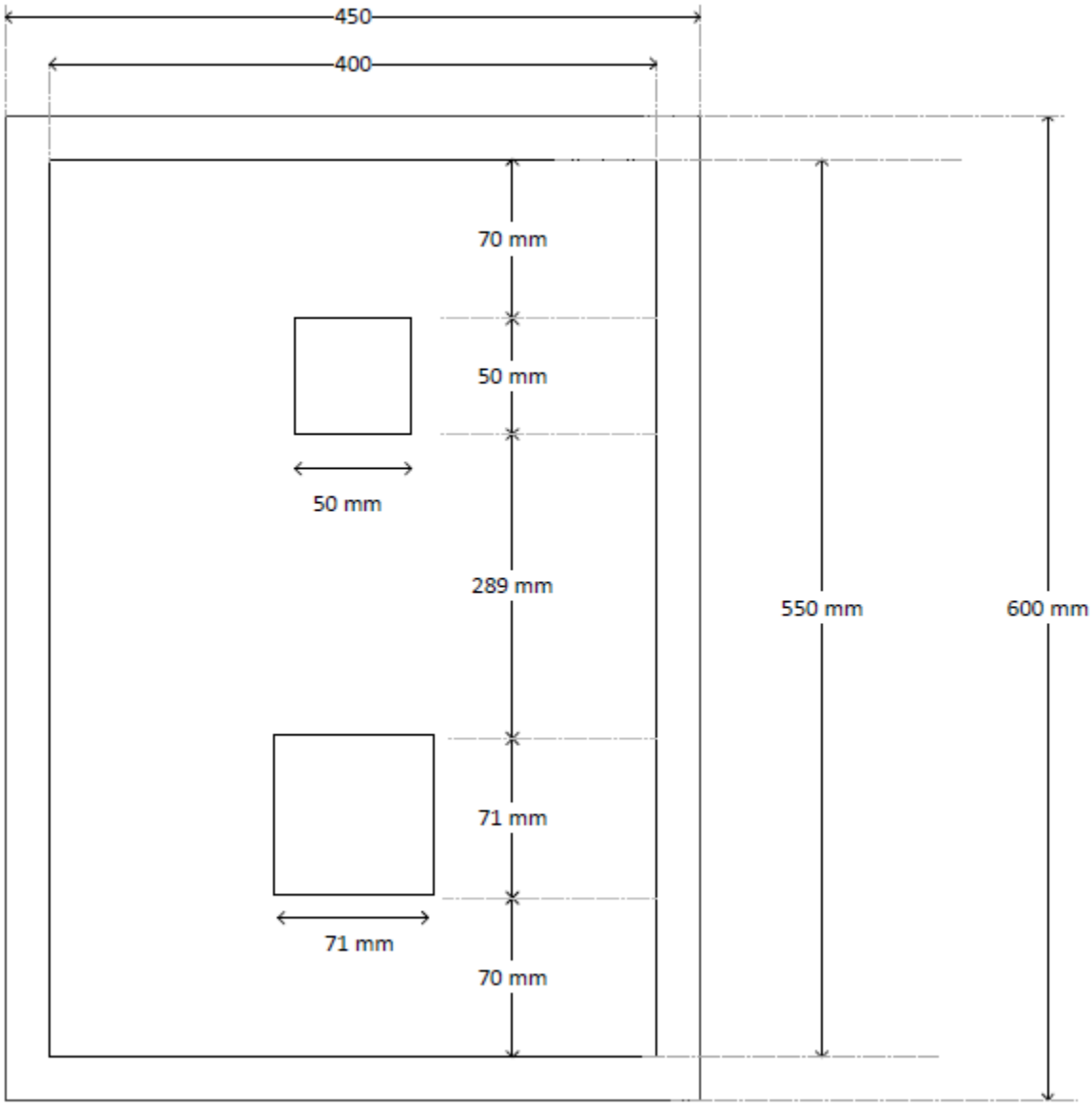

Figure 4.1: Dimensions of screen

The 5 x 5 cm and 7.1 x 7.1 cm gap contained a 32 cm^{-1} mesh count (32 threads per cm). The two gaps can be used to create either a 25 cm^2 or a 50 cm^2 CCM. In order to create a 25 cm^2 CCM, the equipment was setup such that the squeegee pushes the catalyst ink

through the 5 x 5 cm area and a few cm on either side. Prior to the print, 15 x 15 cm sheets of substrate were cut, labelled and weighed. The substrate was held in place by use of a vacuum table.

The final catalyst loading achieved on the substrate was found to be dependent on the catalyst ink rheology and printer operating parameters, namely squeegee pressure, speed and angle. Catalyst loadings of 0.4 $mgPt.cm^{-2}$ were targeted on both anode and cathode.

To achieve good reproducibility, the catalyst ink was applied immediately to the substrate following preparation. This was to avoid evaporation of the solvents which would alter the ink rheology and flow properties.

The printed substrate was allowed to dry overnight in air at room temperature.

4.1.4 Decal transfer

A Carver twelve ton, manual, four-column hydraulic hot press was used to decal transfer two coated substrates onto either side of a N212 membrane.

The two substrates were manually aligned with a 8.5 x 8.5 cm membrane and placed between two 15 x 15 x 1 cm stainless steel plates. 100 µm NOWOFLON PFA sheets were placed between the substrate and the stainless steel. The plates were placed in the hot press at least 30 min prior to the pressing, allowing the temperature to equilibrate. Hot pressing was then carried out under the conditions summarised in Table 4.2.

Table 4.2: Decal transfer conditions

Condition	Value
Temperature	130 °C
Pressure	20000 kPa
Time	180 s

Following hot pressing, the plates were immediately removed from the hot press and allowed to cool off at ambient conditions. In order to complete the decal transfer, the substrate is peeled off leaving the three layered CCM.

The CCM were stored in a plastic sleeve in a specific work desk.

4.1.5 MEA fabrication

The CCM were either assembled into a MEA by placing two GDLs on either side during fuel cell assembly, or by hot pressing two GDLs on either side of the CCM. The hot pressing step was performed at a pressure of 5000 kPa, a temperature of 130 °C and for a duration of 180 s.

4.2 Ex-situ characterisation

In order to better understand the screen printing process and parameters, ex-situ characterisation techniques were employed to study the catalyst ink, printed substrate and CCM. These are described below.

4.2.1 Catalyst ink characterisation

The rheological properties of the catalyst inks were characterised using an AR 1500 EX rheometer, with a 60 mm 0.5° cone. Following ink preparation, approximately 0.5 ml of ink (enough the cover the area below the cone) was placed on the flat base of the rheometer and a 500 μm gap was set between the flat plate and the cone.

The following stepwise flow procedure was then applied:

- 10 s rest
- Shear rate increased from 0 – 800 s^{-1} over 30s
- Shear rate kept constant at 800 s^{-1} for 2 min
- Shear rate decreased to zero over a relatively short time period

The shear stress and shear rate was recorded at various intervals of the process. From this data, the viscosity was obtained.

4.2.2 Optical microscopy

Optical microscopes use visible light and a system of lenses to magnify images of a sample. The image from the microscope can be captured by a light sensitive camera to create a micrograph. Important properties of the applied catalyst layer can be seen with an optical microscope, such as the evenness and smoothness of the coasting. In particular cracks, bubbles and agglomerates on the catalyst layer surface can be observed.

Optical images were taken of the dried catalyst layer on the substrate, using a Wild Heerbrugg M400 microscope with a Zeiss AxioCam camera. The magnifications used were 6.3x and 32x. The sample was flooded with enough light, such that the surface properties were visible.

4.2.3 Scanning electron microscopy

Cross sectional SEM images were used to characterise the smoothness and thickness of the catalyst layers after transfer onto the membrane. The samples were prepared by freezing and breaking under liquid nitrogen, without making contact with the edge that will be observed by the SEM. The sample was then placed in a Nova NanoSEM 230. A magnification of 1500x was used for cross sectional images.

4.3 Fuel cell MEA in-situ characterisation

In-situ MEA characterisation was conducted by assembling and testing the MEA in a commercial fuel test fixture and test station. The procedure is described in detail below.

4.3.1 Test fixture

All MEAs were assembled in a Baltic Fuel Cell test fixture, model number cF25/100 LT V1.1. The test fixture consisted of graphite based 5-fold mixed serpentine flow fields, heating plates and current collector plates. The flow channels have a depth and width of 1 mm. The compression of the test fixture was achieved using a pneumatic actuator.

Before assembly, the flow fields were cleaned using isopropanol and a lint free cloth. The CCM was then sandwiched between two commercial carbon fibre GDLs.

4.3.2 Test station setup

The fuel cell was then connected to a Fuelcon test station (C50-LT). The test station includes the following components:

- electronic mass flow controllers
- heated and insulated gas feed lines
- electrical heating and control system
- external humidification system
- electronic load (TrueData-LOAD®)
- pressure control system
- computerized data acquisition system

Hydrogen, 99.999% pure, from an electrolyser (Hogen ® S Series 2) was fed to the anode side, while oxygen with a purity of 99.998% or synthetic air with a purity of 99.9999% was fed to the cathode side. Humidification of the feed gases was achieved by passing the feed gases through a built in saturator prior to entering the fuel cell.

4.3.3 Fuel cell start-up and pre-test diagnostics

The start-up procedure for the fuel cell is presented below.

The fuel cell was placed on the test station bench and the following connections were made; (i) sense cables to measure cell voltage and current, (ii) air supply for the pneumatic actuator, (iii) anode and cathode feed lines and exhaust lines and (iv) load connecting cables to the current collector plates of the test cell fixture.

The air pressure for the actuator was increased in increments of 0.6 bar to a final pressure of 4.8 bar. This corresponds to a cell compression pressure of 1.5 Nm m^{-2}. This

was followed by a leak test for both anode and cathode. The leak test entailed feeding nitrogen to both the anode and cathode and closing the inlet and exhaust valves to trap nitrogen gas at a higher pressure than atmospheric pressure, approximately 1.8 bar. The pressure was monitored for 5 min and pressure drop of less than 0.035 bar over this period was deemed acceptable.

4.3.4 Fuel cell conditioning

The cell was first purged with nitrogen and the pressure was then set to 2 bar. This was followed by a 15 min heating period to allow the cell to reach 80 °C. The feed lines were set to at least 2.5°C higher than the cell temperature. Once the set operating conditions were reached, hydrogen and oxygen were fed to the anode and cathode respectively. The feed gas specifications are summarised in the table below.

Table 4.3: Feed gas specifications

	Anode	**Cathode**
Gas	Hydrogen	Oxygen
Stoichiometric ratio, λ	1.5	10
Minimum flow rate	0.05 l/min	0.10 l/min
Relative humidity	80%	50%
Saturator temperature	64 °C	49.5 °C

The fuel cell was then left to condition with following set points described in Table 4.4:

Table 4.4: Conditioning set points

Set point	**Time**
Open circuit voltage	5 min
0.6 V	30 min
400 mA.cm^{-2}	Approx 12 hour

After at least 12 hours and once the voltage had stabilised while the current was at 400 mA.cm^{-2}, electrochemical characterisation was performed.

4.3.5 MEA testing: polarisation curves

Polarisation curves were recorded immediately after completion of the conditioning procedure. The reactant flow rates during the data acquisition were load following i.e. based on the electrical current drawn from the cell. The operating conditions for testing are summarised below:

Table 4.5: Polarisation curve operating conditions

Variable	Set point
Temperature	80 °C
Pressure	1 barg
Relative humidity	80/50% at anode/cathode
Stoichiometric ratio, λ	1.5/10 of hydrogen and oxygen

Data points were recorded by measuring the voltage three times at a given current density and taking the average. The current was incrementally increased in steps of 0.5 A in the activation region and 1.5/2 A in the ohmic region. The current was increased until a voltage of 0.45 V was measured, after which the current was decreased back to 0. This procedure was repeated three times. Between each polarisation curve, OCV was maintained for 10 min. OCV is the open circuit voltage and can be considered the maximum potential of the circuit.

4.3.6 MEA testing: electrochemical impedance spectra

EIS data was obtained in galvanostatic mode by applying a current perturbation at different frequencies ranging from 0.1 Hz to 20 000 Hz. At each frequency, the electrical response, real and imaginary, was recorded.

EIS was measured at current densities of 100, 200 and 400 $mA.cm^{-2}$. A rest period of 1 hour was maintained prior to measurement at each current density.

4.3.7 Shutdown procedure

The system was first returned to OCV. The humidifiers were then switched off and bypassed, and the gas lines were purged with nitrogen for 10 min. The temperature of the heating lines was then reduced to allow the system to cool down to ambient conditions and finally the back pressure was reduced to ambient pressure. The MEA was then removed from the cell fixture.

4.4 Commercial MEA

Commercial CCMs were used to (i) benchmark the performance of in-house MEAs and (ii) show the effect of hot pressing vs. no hot pressing of GDLs onto the CCM. Table 4.6 provides a summary of the commercial CCMs used.

Table 4.6: Commercial MEAs

Manufacturer	Baltic	Ion Power	Johnson Matthey
Membrane	N 212	N 212	unknown
Anode loading	0.3	0.5	0.4
Cathode loading	0.6	0.5	0.4

5 Results and Discussion

The major findings of this study are presented and discussed in this section. This includes the catalyst ink characterisation, effect of different screen printing parameters on the printing process and the performance of the MEAs in a fuel cell environment.

5.1 Catalyst ink rheology

A number of different catalyst ink formulations were initially investigated for the printing process. The inks differed with respect to the type and amount of organic solvent, and in one case the amount of de-ionised water. The amounts of catalyst and ionomer solution were kept constant. The different ink formulations are shown in Table 5.1. All inks were prepared as described in Section 4.1.2.

Table 5.1: Different catalyst ink formulations

Component	Ink 1	Ink 2	Ink 3	Ink 4	Ink 5	Ink 6
40 wt% Pt/C	1 g	1 g	1 g	1 g	1 g	1 g
15 wt% ionomer solution	2.8 ml	2.8 ml	2.8 ml	2.8 ml	2.8 ml	2.8 ml
Deionised water	0.5 ml	0.5 ml	0.5 ml	0.5 ml	0.5 ml	3 ml
1,2-Propanediol	1 ml	3 ml	1 ml	1.5 ml	2 ml	2 ml
Isopropanol	0.5 ml	0.5 ml				

Figure 5.1 illustrates the rheological behaviour of the different catalyst inks. At low shear rates (up to about 300 s^{-1}), the viscosity decreases non-linearly. At higher shear rates the viscosity continues to drop, but at a less rapid rate. This rheology profile is similar to the expected profile in Figure 2.9. However, the tight packing of molecules, leading to an increased viscosity was not observed as a higher shear rate is required for this phenomenon to occur.

As an initial screening process, the 6 different inks were used for screen printing. Ink 1 was found to be too viscous and did not flow through the holes of the mesh on the screen. The viscosity of ink 6 was found to be too low, close to that of water, and continued to spread on the substrate following the printing. Inks 2-5 were found to pass through the mesh and leave a stable print on the substrate. These ink formulations were therefore further investigated.

The rheological behaviour of inks 2-5 at low shear rates is shown in Figure 5.2. In the screen printing process, the catalyst ink typically experiences shear rates of 0-300 s^{-1} and hence this is the range shown.

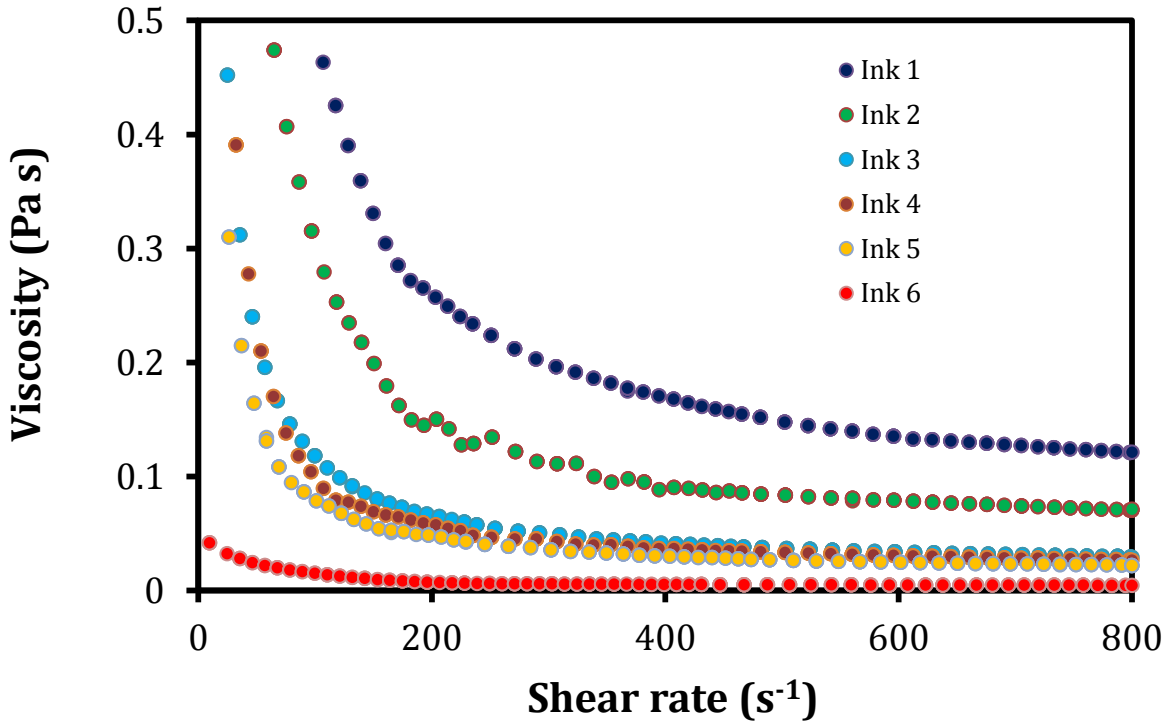

Figure 5.1: Plot of viscosity versus shear rate for different ink formulations

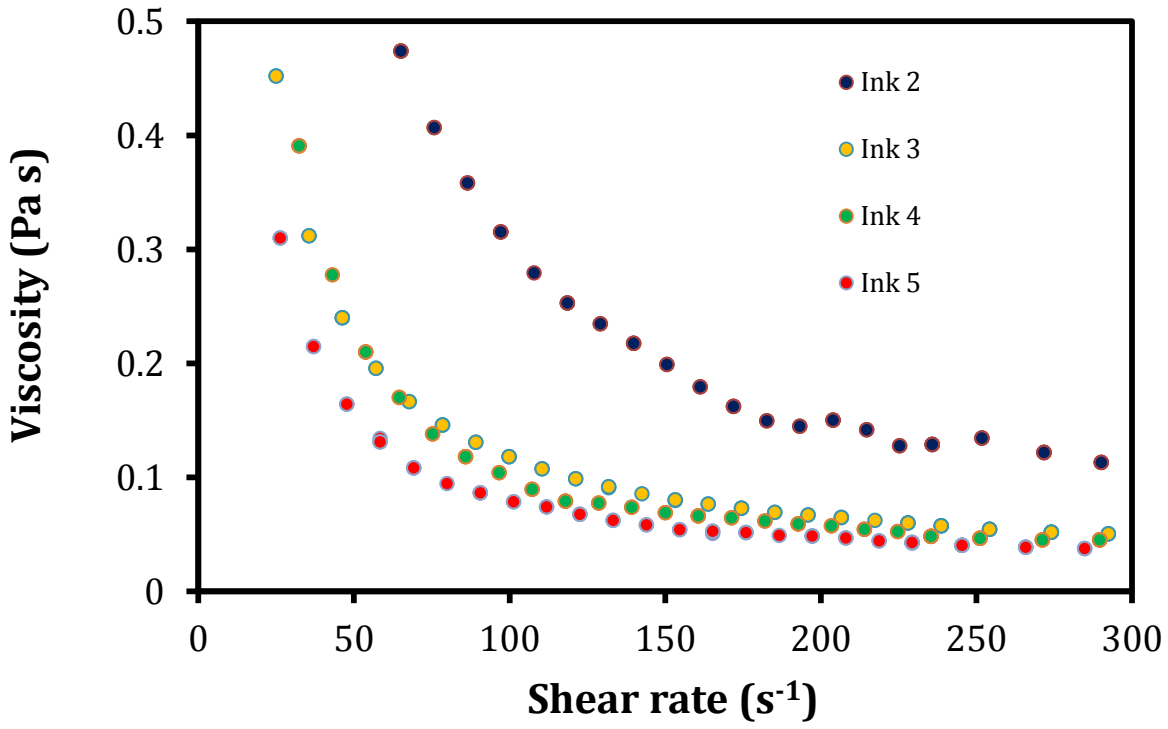

Figure 5.2: Plot of viscosity versus shear rate for successful ink formulations

The viscosity at all shear rates decreases slightly from ink 3 to 5. For these inks, the solvent type was kept constant and the solvent volume was increased. Therefore as expected, with increasing solvent volume and therefore decreased solids content the ink viscosity decreases. In the preliminary screening process, inks 3-5 were found to yield a smooth printed surface.

Ink 1 and 2 show a significantly higher viscosity than inks 3-5 at all shear rates. This is indicative of a more dispersed ink and is attributed to the presence of the isopropanol in addition to the 1,2-propanediol. Based on the trend of decreasing viscosity with increasing 1,2-propanediol for inks 3-5, more 1,2-propanediol was added to ink 1 to develop the suitable ink 2.

Given the similar rheological behaviour of inks 3-5, only inks 2 and 3 were further investigated and characterised for screen printing and fuel cell testing. Figure 5.3 shows an optical image of the resultant printed substrates from ink 2 and ink 3.

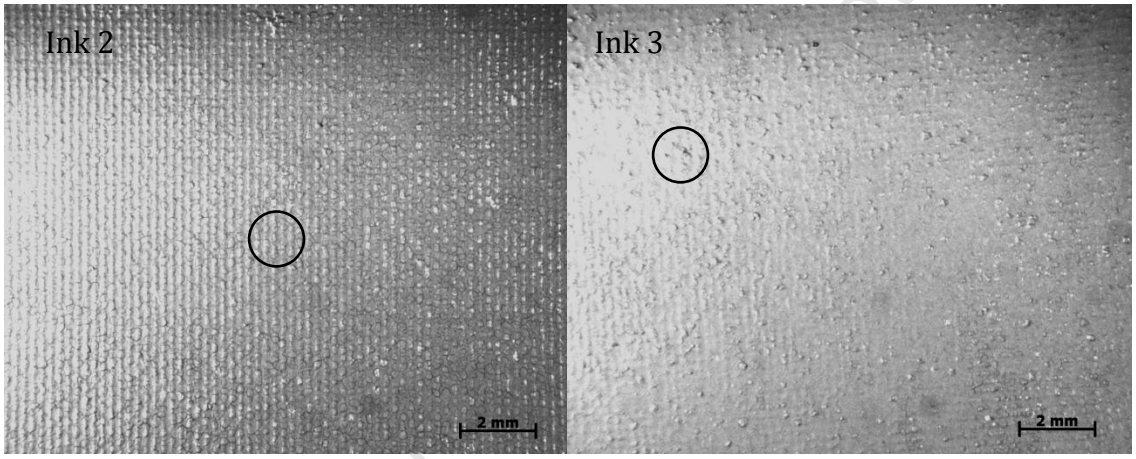

Figure 5.3: Optical microscopic images for two different ink formulations

The indicated spot on both pictures in Figure 5.3 are used to compare the printed surface. Ink 2 shows a series of vertical and horizontal grooves of even spacing, indicating the mesh wiring of the screen. It also shows a very even print and that the print has not continued to run after the process. Ink 3 also shows the same outlines of the mesh, but not as clear. Although a consistent print, with no macroscopic deformations and cracks, microscopic imaging reveals the presences of inconsistent bumps. This is indicative of agglomeration, reinforcing the notion that isopropanol acts as a dispersant.

Figure 5.4 shows SEM images of the resultant catalyst coated membranes formed from decaling printed substrates from ink 2 and 3.

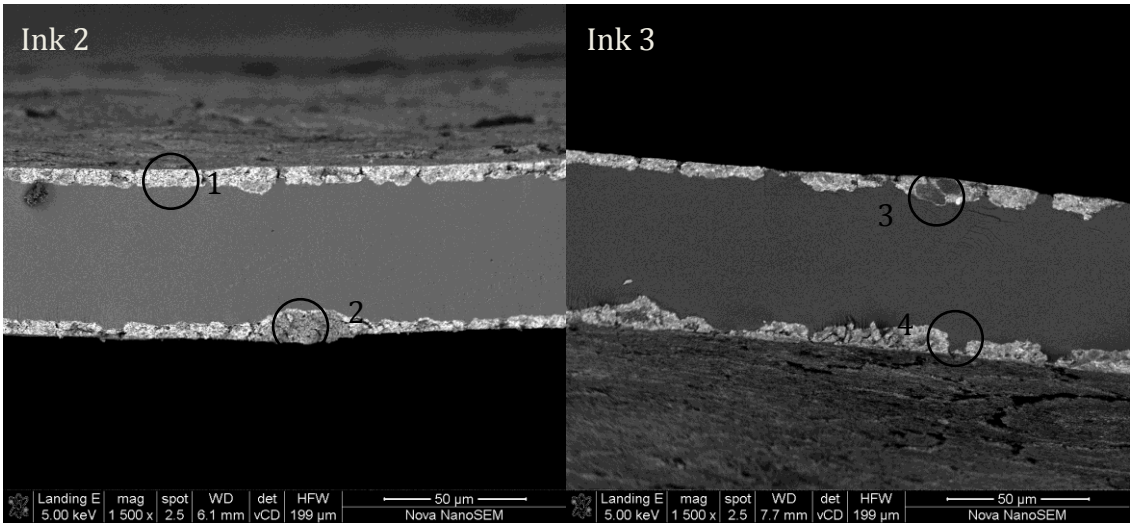

Figure 5.4: SEM images of CCMs made from different ink formulations

Spot 1 shows the evenness of the catalyst layer using ink 2. Spot 2 shows the inconsistencies on the surface, and this point is considered the maximum thickness of the layer. Based on the SEM image, the catalyst layer ranges from approximately 5 – 20 µm in thickness, consistent with literature examples (Lim et al., 2012).

Spot 3 shows a fairly thick section of the catalyst surface, while spot 4 shows a section almost devoid of catalyst on the membrane. These indicate a poorly coated membrane, revealing that the performance of ink 2 should be better than that of ink 3 due to the consistency of the print and therefore better utilisation of the catalyst.

5.2 Screen printing parameters

Two screen printing parameters, namely printing speed and printing pressure and angle were considered and are presented below.

5.2.1 Printing pressure and angle

The printing pressure affects the shear stress that is applied to the catalyst ink, which in turn affects how much ink, of a certain viscosity, will flow through the mesh of the screen. If the pressure is too low, not enough or no ink will flow through the mesh, resulting in a 'poor' print. At a certain pressure, the mesh will be filled with the maximum possible ink, resulting in a successful print. If the pressure is increased above this point, no further change in the print is observed. A certain pressure is therefore required to overcome the friction force and force the ink through. The two factors affecting the printing pressure are the squeegee pressure and angle.

A squeegee pressure of 4.1 bar is the maximum for the screen printing equipment used in this study. It was found that for the ink used in this study, a pressure of 3.4 bar yielded a successful print.

The printing angle range is between 15° and 35°. By increasing the angle, the resultant force decreases and the contact surface area increases. If the contact area is too high, the advantage of using a sharp squeegee edge is lost. An angle of 22° was found to be optimal for the catalyst inks used in this investigation. The characterisation was done by visual inspection and optical microscopy.

5.2.2 Printing speed

Various printing speeds were considered for a certain pressure and angle setting on the printer. The speed at which the print takes places affects the shear rate that the catalyst ink undergoes. An increased speed leads to an increased shear rate. This in turn affects the required ink viscosity during printing process. This aspect is illustrated in Figure 5.5.

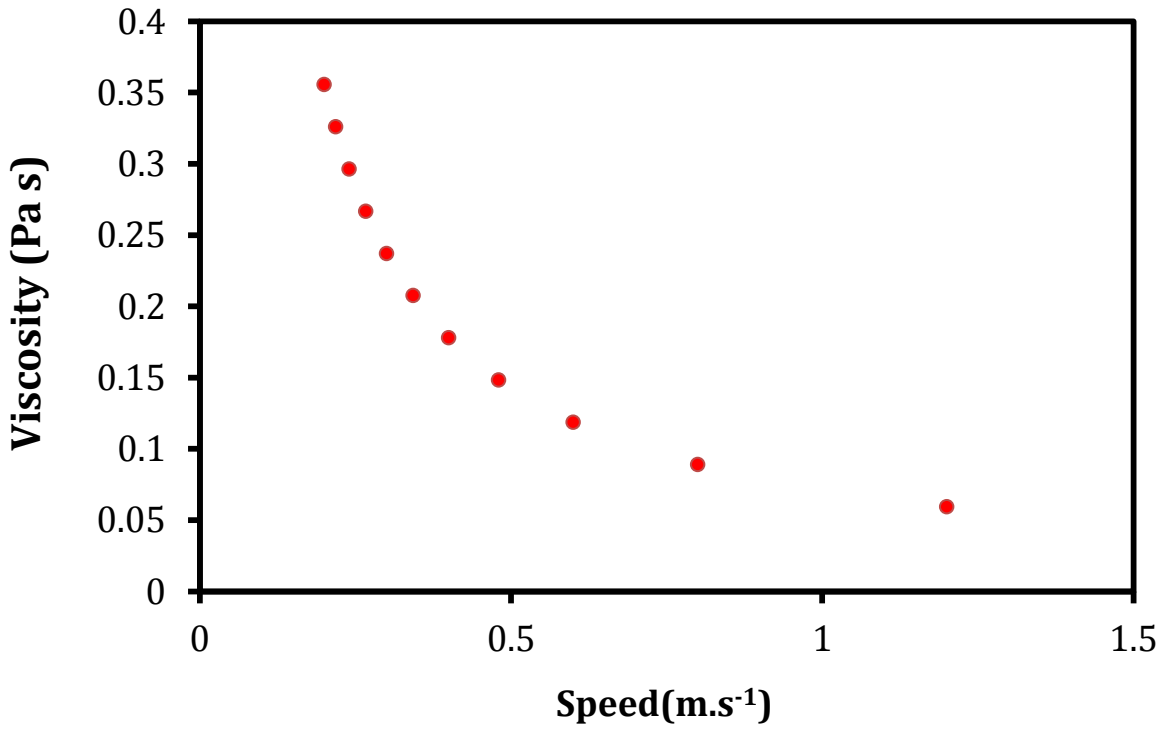

Figure 5.5: Relationship between desired speed and viscosity

The data presented in Figure 5.5 is estimated from the force balance and viscosity definitions. Without measuring shear stress during the actual print it is impossible to use this data as anything more than just a rough guideline. What one can gain form this work is that for a very thin ink, a faster speed is required, while for a thick ink, a slower speed is required. For the case of ink 2, the printing speed of 0.6 $m.s^{-1}$ was found to be

ideal. This coincides with a viscosity of approximately 1.12 Pa.s, agreeing with the rheology profile shown in Figure 5.2. It is therefore important to have an understanding of both the rheology profile and the printing parameters in order to have a successful print.

For printing speeds higher than 0.6 $m.s^{-1}$, the ink would not have flowed through the mesh due to the lower viscosity requirement, resulting in a poor print as shown below in the microscopic image in Figure 5.6.

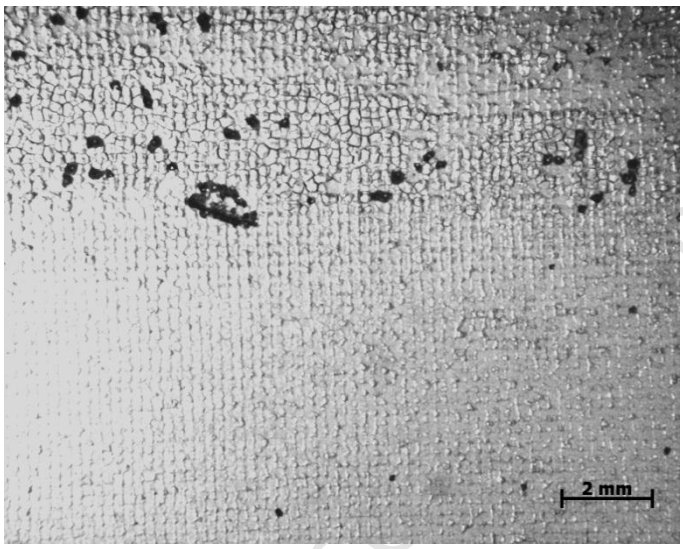

Figure 5.6: Result of incorrect printing speed

Figure 5.6 shows various pin holes and regions where the substrate was not covered or printed on due to an incorrect printing speed for ink 2.

5.2.3 Printer performance summary

The quality of the screen print coating is strongly dependent on the ink rheology and the specific settings on the printer. The catalyst ink is required to be within a certain viscosity range or printing cannot occur. Optimisation of the printer settings is required for each catalyst ink, depending on its rheology profile. For a well dispersed catalyst ink, such as ink 2, the optimal conditions were found to be 3.4 bar at 22° and a speed of 0.6 $m.s^{-1}$.

5.3 Fuel cell testing

5.3.1 Reproducibility

The reproducibility of the testing procedure and equipment was investigated by performing three polarisation curve measurements on a single MEA. Figure 5.7 shows the three polarisation curves.

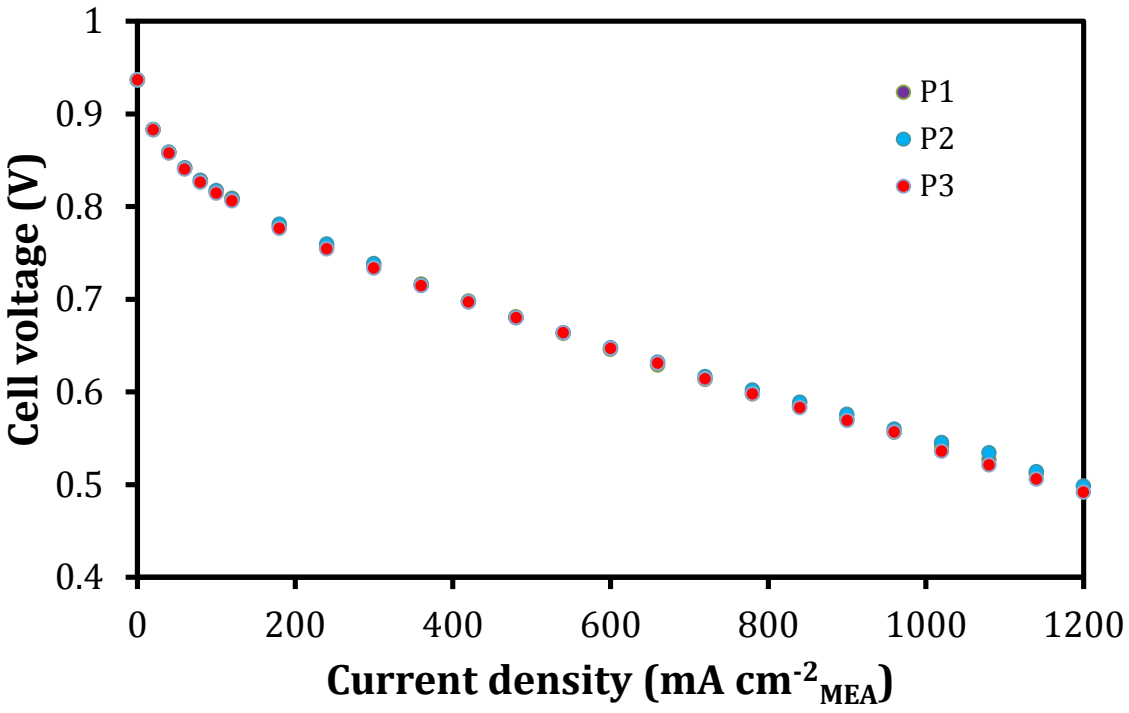

Figure 5.7: Polarisation curves showing three polarisation curve measurements for a single MEA (T = 80 ^{0}C, P = 2 bar, s $_{hydrogen}$ = 1.5, s $_{oxygen}$= 10, RH$_{anode}$ = 80% , RH$_{cathode}$ = 50%, catalyst loading = 0.32 mg Pt. cm^{-2})

Table 5.2 shows the average and percentage (deviation) of the cell voltage at each current density. These values indicate a high level of reproducibly with a maximum deviation of 3.29% at 1080 mA.cm^{-2}. The higher deviation at higher current and therefore flow rate of reactant gases are expected due to fluctuations of the flow rate around the set point.

The high level of reproducibility in this data installs confidence in the test station as well as the other data obtained.

Table 5.2: Average voltages and percentage deviations for three polarisation curve measurements.

i(mA cm^{-2}$_{MEA}$)	V_m(V)	σ_v	μ(%)
0	0.93	0.006	0.09
20	0.88	0.008	0.09
40	0.85	0.007	0.25
60	0.83	0.007	0.34
80	0.82	0.007	0.62
100	0.81	0.006	0.68
120	0.80	0.007	0.78
180	0.77	0.005	1.15
240	0.75	0.005	1.26

$i(mA\ cm^{-2}_{MEA})$	$V_m(V)$	σ_v	$\mu(\%)$
300	0.73	0.005	1.15
360	0.71	0.005	0.41
420	0.69	0.005	0.25
480	0.68	0.005	0.28
540	0.66	0.002	0.19
600	0.64	0.004	0.41
660	0.63	0.009	0.75
720	0.61	0.009	0.78
780	0.59	0.010	1.14
840	0.58	0.012	1.55
900	0.56	0.010	1.69
960	0.55	0.007	1.00
1020	0.54	0.006	2.33
1080	0.52	0.008	3.29
1140	0.51	0.004	2.05
1200	0.50	0.005	2.44

5.3.2 Reproducibility of MEA preparation

The reproducibility of the preparation procedure was investigated by comparing four MEAs from two subsets. Two of the MEAs were prepared using ink 3 (MEA-1 and MEA-2) and the other two using ink 4 (MEA-3 and MEA-4). Figure 5.8 presents the polarisation curves of the four MEAs. The polarisation curve shown for each MEA is an average of at least three polarisation curves, and therefore each curve is presented with its respective standard deviation.

Figure 5.8 shows that in both cases, very good reproducibility is observed at all current densities for distinct MEAs prepared using the same ink recipe. These results show the reproducibility of the catalyst ink preparation, screen printing and decal transfer procedures. With a reproducible procedure established for the CCM technique, further work modifying the catalyst layer and MEA can be done due to the ability to differentiate MEAs.

Ink 3 has a higher solids content, leading to an increased amount of catalyst per unit volume and therefore per mesh hole. This in turn leads to a higher loading and hence an improved performance. The loading on the MEA can therefore be controlled by varying the solid content in the catalyst ink.

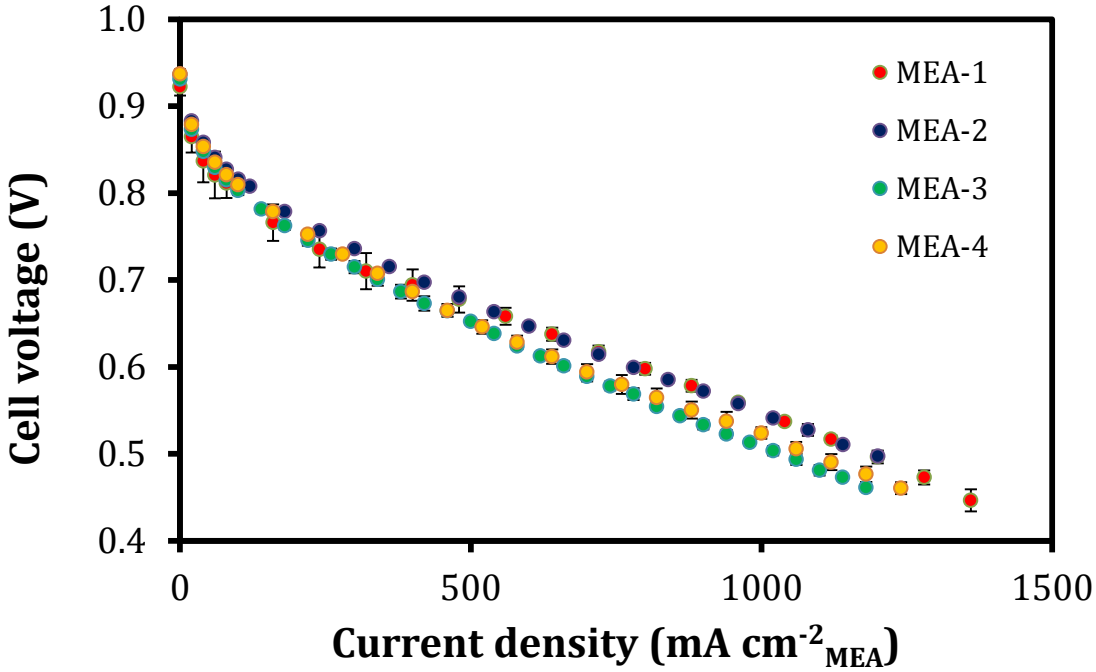

Figure 5.8: Polarisation curves of 4 distinct MEAs (T = 80 ^{0}C, P = 2 bar, s $_{hydrogen}$ = 1.5, s $_{oxygen}$= 10, RH$_{anode}$ = 80% , RH$_{cathode}$ = 50%, catalyst loading = 0.35 mg Pt.cm^{-2} (MEA 1 and MEA2) and 0.32 mg Pt. cm^{-2} (MEA 3 and MEA 4))

5.3.3 Comparison with commercial MEA

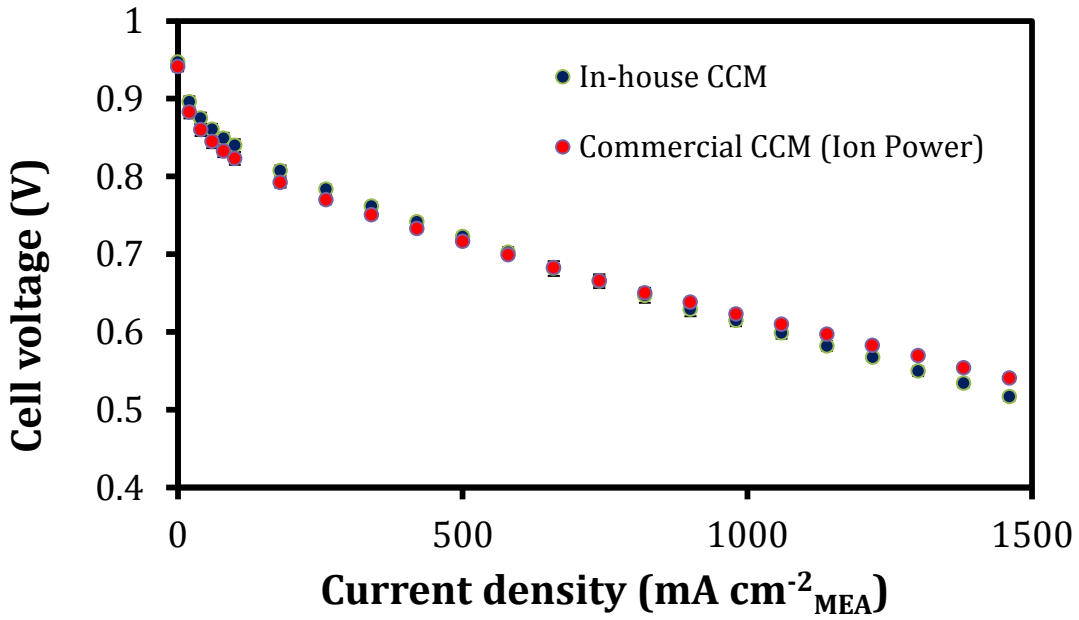

Figure 5.9: Comparison of performance commercial and in house CCMs (T = 80 ^{0}C, P = 2 bar, s $_{hydrogen}$ = 1.5, s $_{oxygen}$= 10, RH$_{anode}$ = 80% , RH$_{cathode}$ = 50%, catalyst loading = 0.5 mg Pt.cm^{-2})

Figure 5.9 compares the performance of an in-house CCM with a commercial CCM with the same catalyst loading, membrane and GDL. The results of the EIS measurements at 400 mA.cm^{-2} are presented in Figure 5.10. The resistance and capacitance values obtained by fitting the data to an equivalent circuit are presented in Table 5.3.

Figure 5.9 shows similar fuel performance at all current densities for the commercial and in-house CCMs. The in-house CCM performed slightly better in the activation region, while the commercial CCM performed slightly better in the mass transfer region.

The EIS results show a higher charge transfer resistance in the in-house CCM. The fact that this does not result in the in-house CCM showing a far worse curve performance indicates that another factor in the testing environment may be dominating, resulting in similar overall performance. Because these two MEAs were fabricated in different environments, with different procedures, one can assume that the performance is limited by the testing procedure or equipment. Two probable sources exist: (i) A poorly designed flow field leading to water management problems for both CCMs and (ii) The cell compression in the test is not ideal for the GDL used for both CCMs.

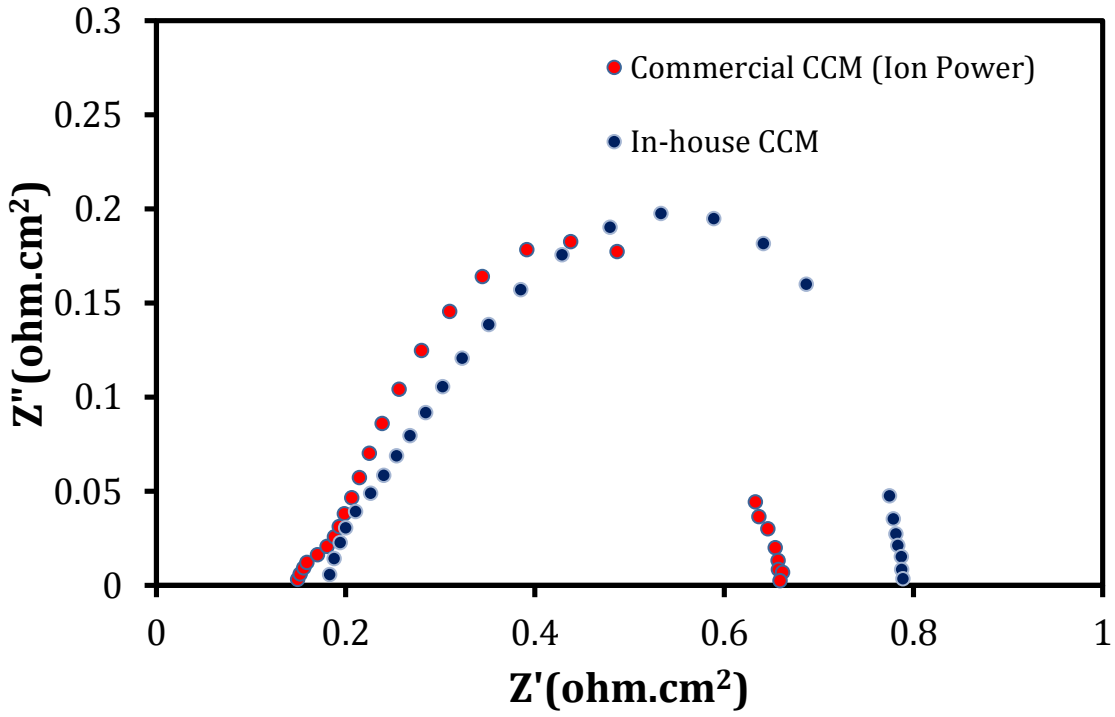

Figure 5.10: EIS comparison between commercial and in house CCMs (T = 80°C, P = 2 bar, s $_{hydrogen}$ = 1.5, s $_{oxygen}$= 10, RH$_{anode}$ = 80% , RH$_{cathode}$ = 50%, catalyst loading = 0.5 mg Pt. cm^{-2}, current density = 100 mA cm$^{-2}{}_{MEA}$)

Table 5.3: Equivalent circuit values for commercial and in-house CCMs

	Rs (ohm.cm²)	Rct (ohm.cm²)	Cdl (F)	n
Commercial CCM (Ion Power)	0.17	0.50	0.0012	0.77
In-house CCM	0.20	0.61	0.00082	0.72

Figure 5.11 compares the performance of an in-house CCM with a commercial Johnson Matthey (JM) MEA. The performance of the JM MEA is far superior to that of the in-house CCM. Various reasons could exists for this including: (i) JM using superior raw materials, (ii) An improved fabrication procedure leading to an increased platinum utilisation and (iii) The commercial MEA being far better suited to the testing environment.

The result also shows that although major improvements have been made at HySA/Catalysis, future research is required to be able to compete with commercial MEAs.

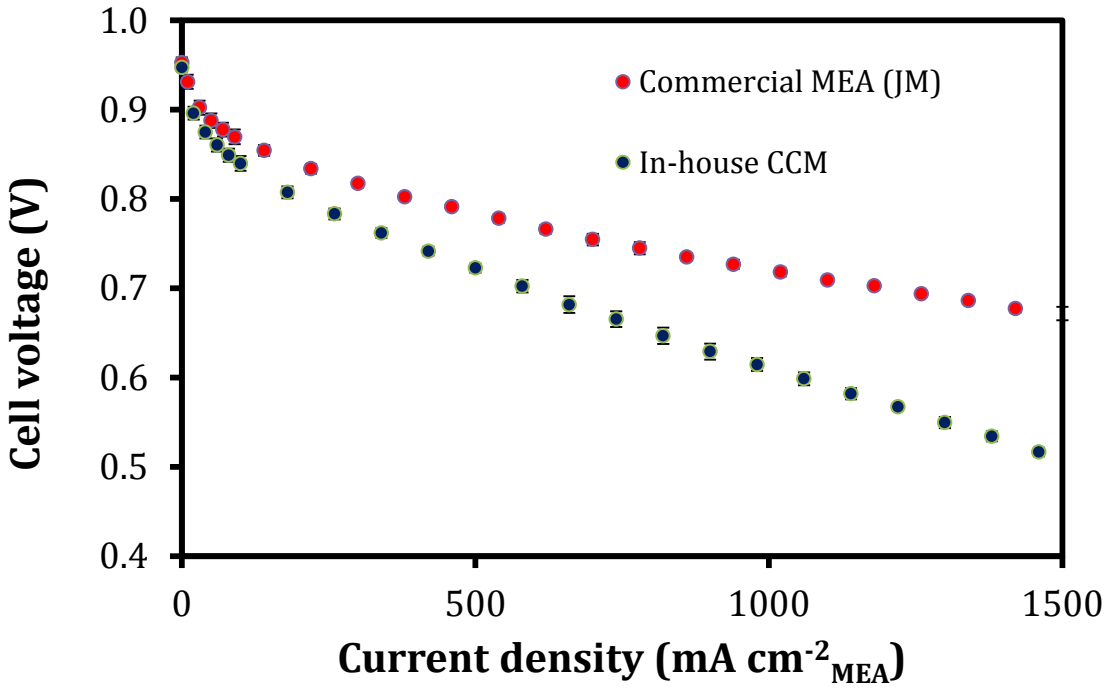

Figure 5.11: Comparison of performance between in-house CCMs and commercial MEA (T = 80 ^{0}C, P = 2 bar, $s_{hydrogen}$ = 1.5, s_{oxygen}= 10, RH_{anode} = 80% , $RH_{cathode}$ = 50%, catalyst loading = 0.5 mg Pt.cm^{-2} (in-house) and 0.4 mg Pt.cm^{-2} (commercial))

5.3.4 Air vs oxygen

Figure 5.12 compares the performance of an in-house MEA when operated with air (21% oxygen) and 100% oxygen at the cathode. The figure also shows a 'model' curve, where the results of the i-R corrected 100% oxygen run were adjusted using the Nernst equation (Eq. 1) and the exchange current density equation (Eq. 15) for a 21% oxygen feed. As expected the performance in 100% oxygen far exceeds that in air. The polarisation curve with air shows the onset of mass transfer limitations at a current density greater 500 mA.cm^{-2}.

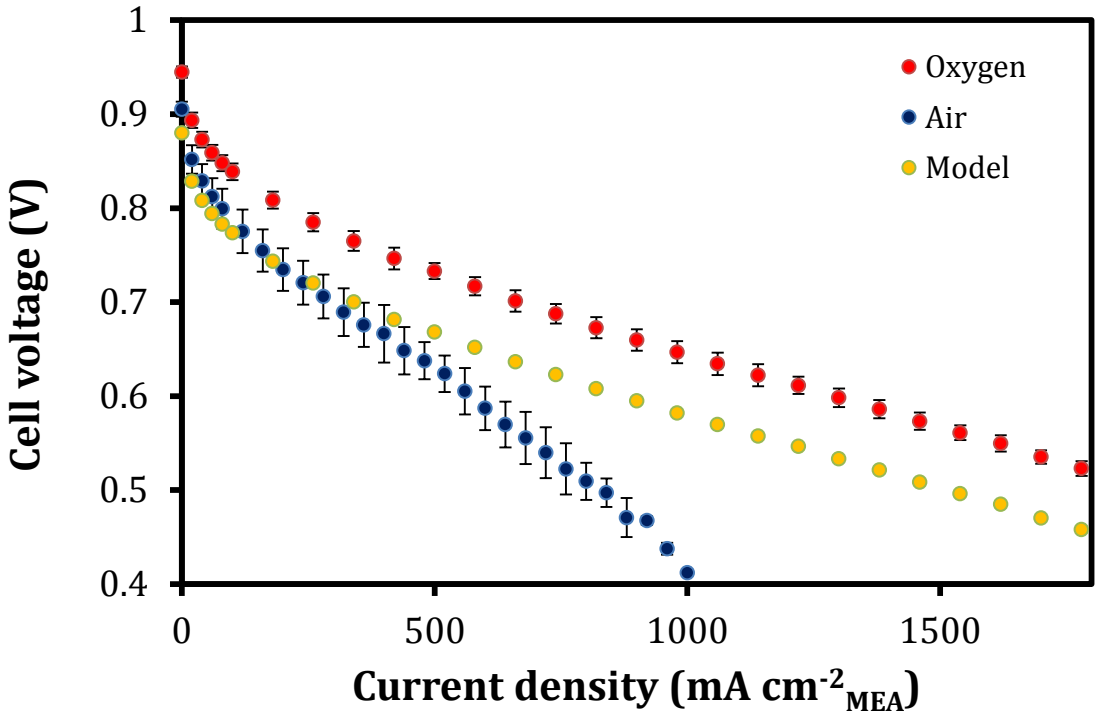

Figure 5.12: Polarisation curve for a single MEA with (i) air and (ii) oxygen at the cathode (T = 80 ^{0}C, P = 2 bar, s $_{hydrogen}$ = 1.5, s $_{oxygen}$ = 10, s $_{air}$ = 2, RH$_{anode}$ = 80% , RH$_{cathode}$ = 50%, catalyst loading = 0.4 mg Pt. cm^{-2})

From the Tafel plot of the oxygen polarisation curve (Figure 5.13), a transfer coefficient of 0.9 was calculated and this value was used for the model curve. The Tafel slope was calculated to be 77 mV.decade^{-1}. Both of these agree with typical fuel cell operation. (Barbir, 2005).

The model prediction of the performance in air is accurate in the activation and ohmic region, but fails to model the mass transfer region. This result is expected because the model is a kinetic model and does not account for mass transfer. It therefore purely models the change in oxygen partial pressure.

The mass transfer limitations arise due to the presence of nitrogen in the synthetic air. The nitrogen blocks the pathway between the oxygen and the active catalyst particles. The reaction therefore proceeds as fast as the oxygen can reach the catalyst. As the current density increases and hence the flow rate increases, the effect becomes more noticeable.

The decrease in performance is however slightly more pronounced than expected when comparing to some of the literature sources (Tang et al., 2007). A possible reason for this is a water management issue. If flooding were to occur, the pores in the GDL and catalyst would be further blocked up, as well as the flow field channels. This effect would result in a further disruption of getting the oxygen to the active catalyst surface.

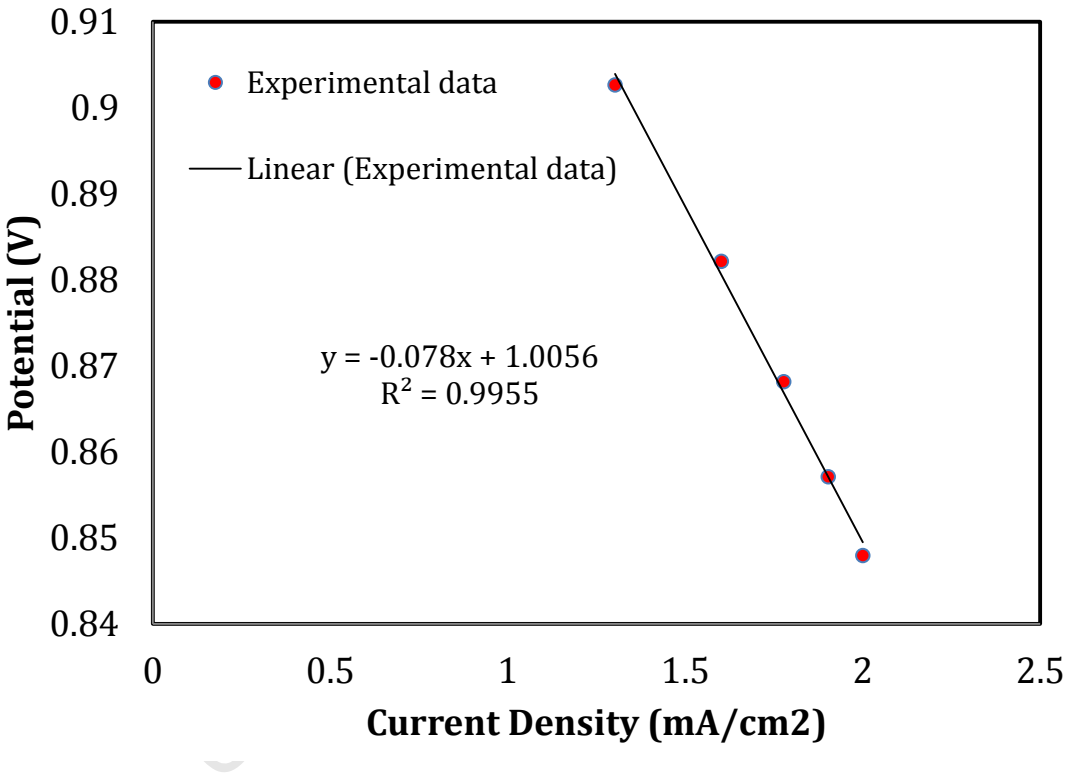

Figure 5.13: Tafel plot for Oxygen kinetic region

5.3.5 Effect of relative humidity

The effect of the relative humidity on the performance of the in-house prepared CCMs was investigate and is compared in Figure 5.14.

Figure 5.14 shows only a slightly improved performance at the higher relative humidities of 80%/50% (anode/cathode). This is slightly surprising as in general, performance is expected to increase significantly with increasing humidification. This is due to an increased catalyst utilisation because of the ionomer becoming more active at elevated humidities (Shinozaki et al., 2011).

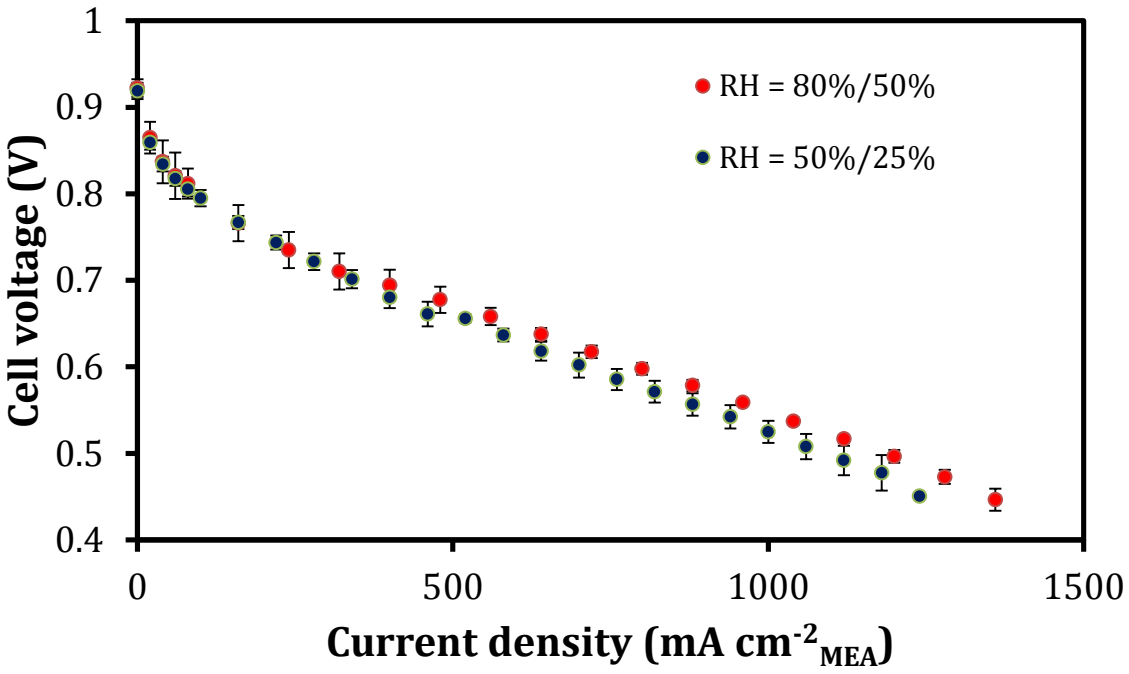

Figure 5.14: Polarisation curves for a single MEA at different relative humidities (T = 80 ^{0}C, P = 2 bar, $s_{hydrogen}$ = 1.5, s_{oxygen}= 10, catalyst loading = 0.4 mg Pt. cm^{-2})

Although increased humidification leads to a more active membrane and ionomer, it needs to be balanced with water management. Aside from the already mentioned blocking of the catalyst pores, and therefore decreasing the active metal sites, certain flow fields are poorly designed to accommodate excess water. The flow field used in this experiment setup is illustrated in Figure 5.15.

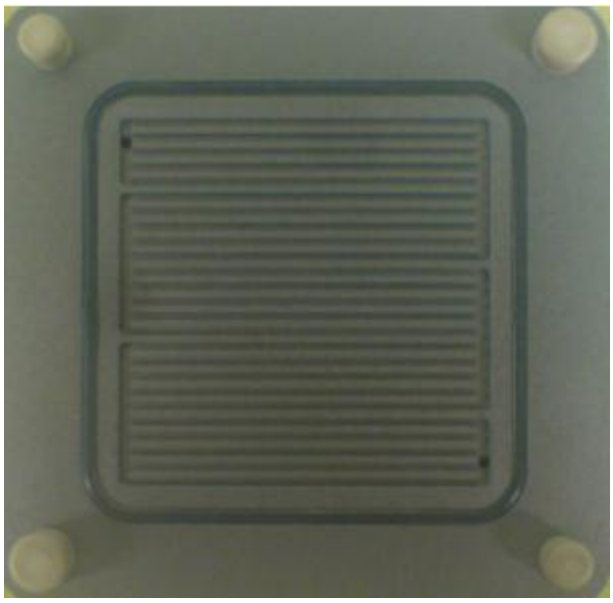

Figure 5.15: 5-fold mixed serpentine flow field design

The serpentine flow field has been shown to offer a decrease in cross over and an increase in fuel utilisation. It has, however, been shown that at higher humidities, it responds poorly to water management. This is due to water droplets in the channels blocking off entire sections of active catalyst. An interdigitated flow field design, depicted in Figure 5.16, can improve the mass transfer of oxygen to the catalyst sides in wet conditions. (Arico et al., 2000). It is possible that due to this cell fixture offering better water management, it may increase the performance of the MEAs made at HySA/Catalysis. It therefore represents an opportunity in which future researchers can investigate.

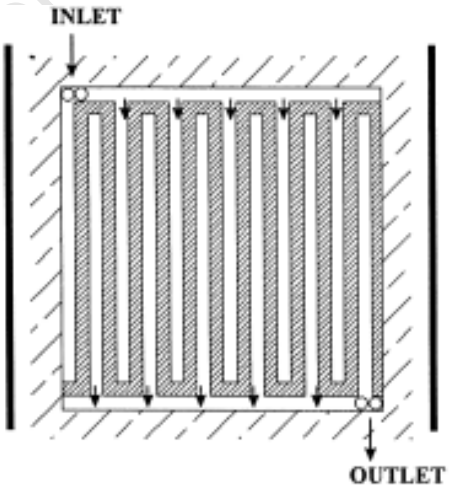

Figure 5.16: Interdigitated flow field design (Arico et al., 2000)

5.4 Variation of MEA preparation parameters

5.4.1 Effect of variation of organic solvent

As discussed in Section 5.1, the result of printing with ink 2 and ink 3 were characterised using optical and SEM imaging (Figure 5.3 and Figure 5.4). The results showed that the addition of isopropanol further disperses the catalyst ink by breaking down agglomerates. In order to further support this claim, two MEAs were made with the same loading and different catalyst inks, ink 2 and ink 3 respectively. The resulting polarisation curve is presented in Figure 5.17.

The result shows that with inclusion of isopropanol, the performance increases by as much as 100 mV. The only difference between to two MEAs was the solvent used, therefore the increased performance points towards an increased catalyst utilisation. This increased utilisation is indicative of a well dispersed catalyst.

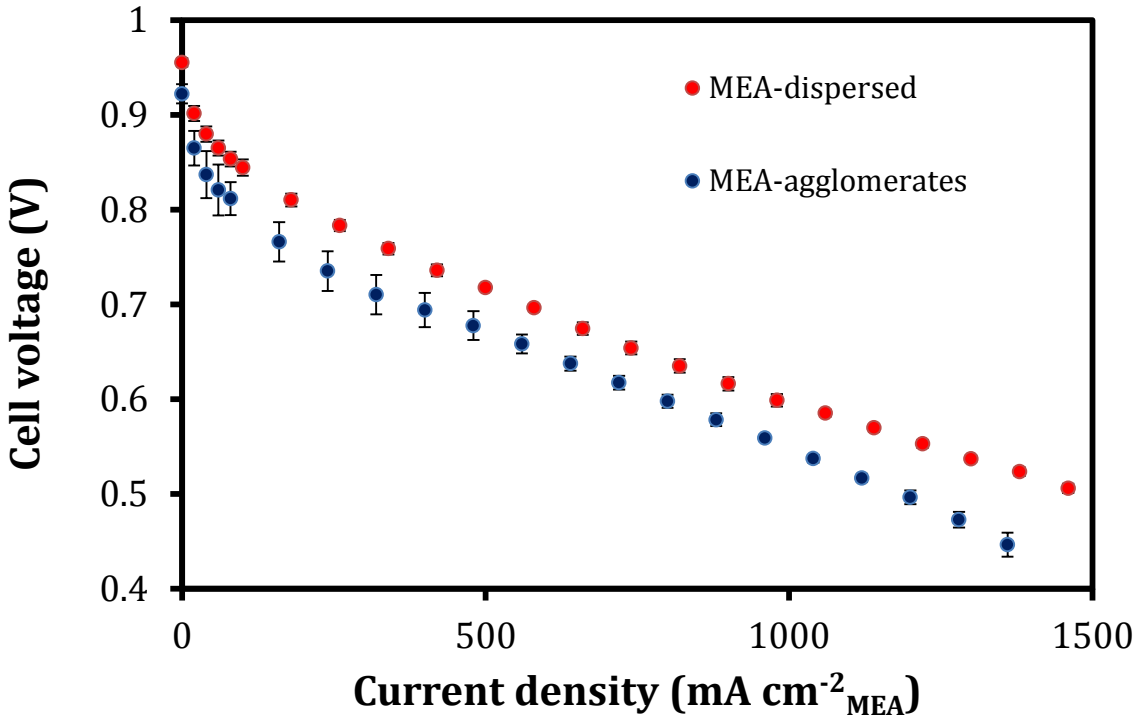

Figure 5.17: Polarisation curve for MEAs prepared with two different catalyst inks (T = 80 ^{0}C, P = 2 bar, s $_{hydrogen}$ = 1.5, s $_{oxygen}$= 10, RH$_{anode}$ = 50% , RH$_{cathode}$ = 25%, catalyst loading = 0.4 mg Pt. cm^{-2})

5.4.2 Effect of hot pressing step

A CCM can either be assembled in a single cell test fixture with or without the GDLs hot pressed on either side. In order to investigate the effect of hot pressing and whether effect changes for different CCMs, commercial and in-house prepared CCMs were tested

with and without a hot pressing step. In all cases the GDL used was Freudenberg. Figure 5.18 shows the effect of the hot pressing step on two different commercial CCMs.

Figure 5.18 shows a slight improvement with hot pressing for the Ion Power CCM and very similar results for the Baltic CCM with and without hot pressing. In general, a minimal effect of hot pressing the GDLs is observed for the commercial CCMs.

Figure 5.19 shows the effect of the hot pressing on the performance on in-house prepared CCMs. EIS measurements were also conducted at a current density of 400 mA cm^{-2} and are presented in Figure 5.20, with resistance and capacitance values presented in Table 5.4.

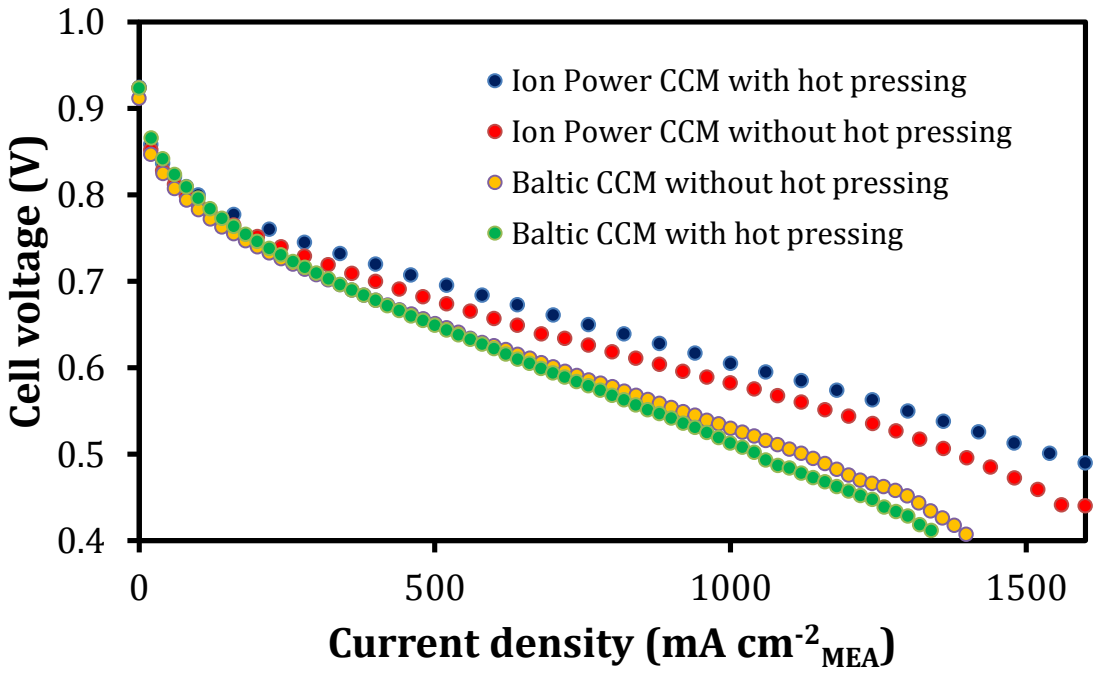

Figure 5.18: Polarisation curves showing effect of hot pressing on the performance of commercial CCMs (T = 70 ^{0}C, P = 1 bar, $s_{hydrogen}$ = 1.5, s_{oxygen}= 2, RH_{anode} = 60% , $RH_{cathode}$ = 0%)

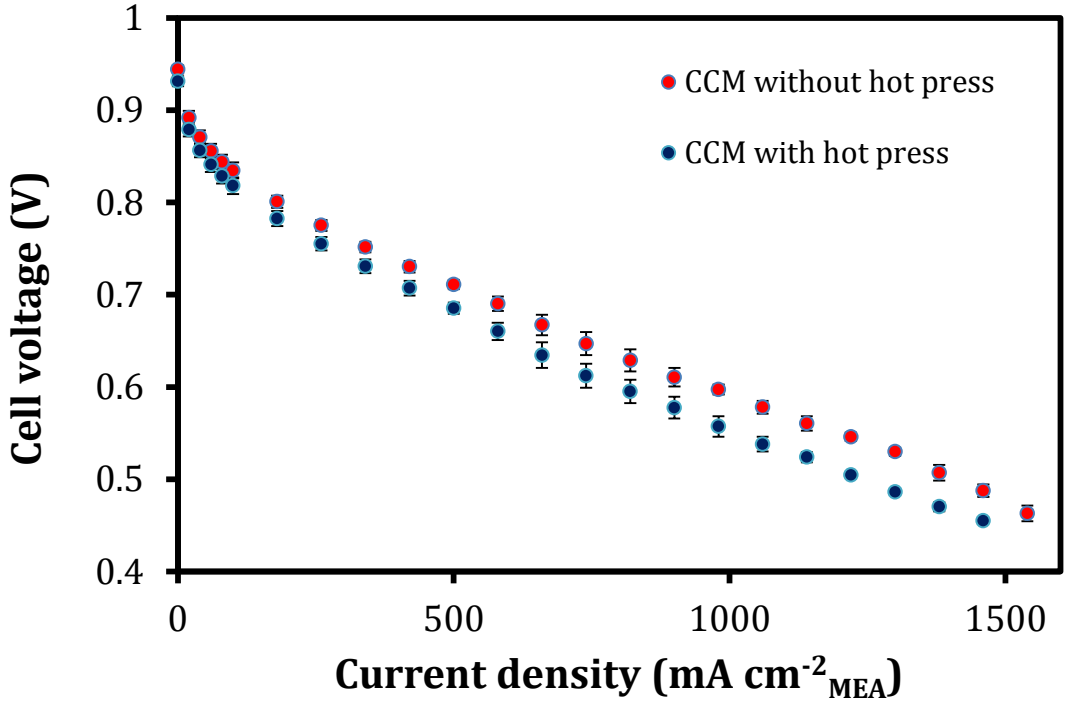

Figure 5.19: Polarisation curve showing the effect of hot pressing on the performance of in-house CCMs (T = 80 ^{0}C, P = 2 bar, s $_{hydrogen}$ = 1.5, s $_{oxygen}$= 10, RH_{anode} = 50% , $RH_{cathode}$ = 25%, catalyst loading = 0.4 mg Pt. cm^{-2})

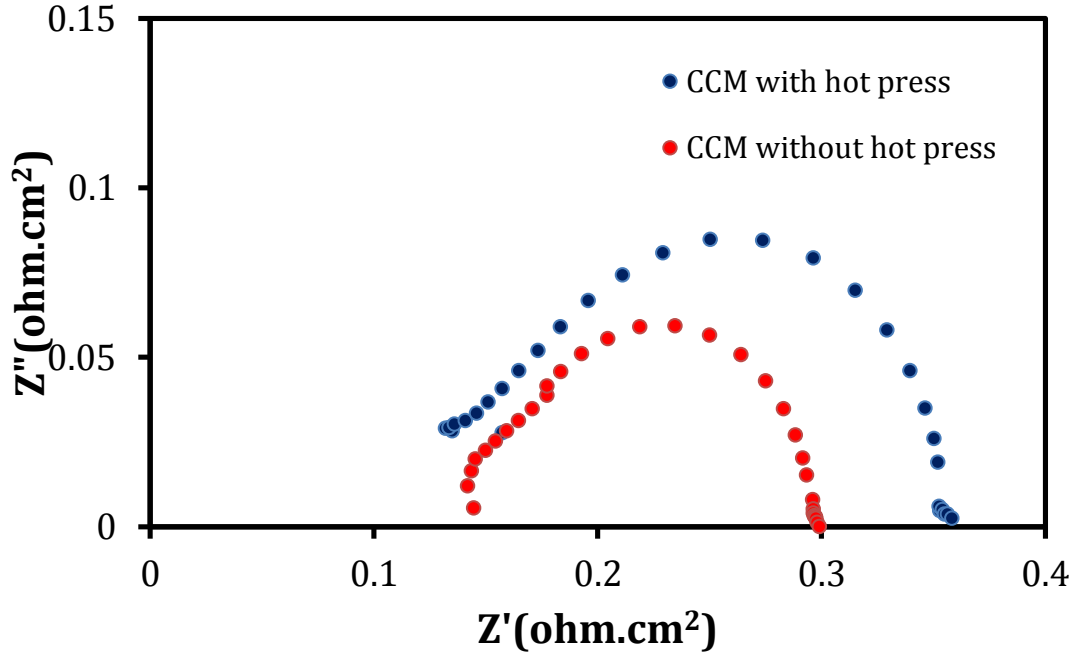

Figure 5.20: EIS showing the effect of hot pressing on the performance of in-house CCMs (T = 80°C, P = 2 bar, s $_{hydrogen}$ = 1.5, s $_{oxygen}$= 10, catalyst loading = 0.4 mg Pt. cm^{-2}, Current density = 400 mA cm$^{-2}{}_{MEA}$)

Table 5.4: Equivalent circuit values showing effect of hot pressing

	Rs (ohm.cm^2)	Rct (ohm.cm^2)	CPE (F)	n
CCM with hot press	0.15	0.21	0.00030	0.86
CCM without hot press	0.14	0.16	0.00064	0.84

Figure 5.19 shows the performance of the CCM decreases with the hot pressing step. The decreased performance can be explained by the EIS results, which show that the inclusion of the hot pressing step results in a higher charge transfer resistance. It is difficult to explain completely why this is the case, but a possible reason may be that some unfavourable modification to the catalyst layer is taking place during the hot pressing step.

This result confirms the process that was suggested in literature (Tang et al., 2007), furthermore establishing the CCM platform for which future researchers can work from. It also significantly cuts down on the time factor benefiting future scale up and commercialisation at HySA/Catalysis.

5.4.3 Effect of different GDLs

Figure 5.21 and Figure 5.22 shows the polarisation curve and EIS results for in-house CCMs assembled with three different commercial GDLs, Table 5.5 shows the resistance and capacitance values when modelling the system as an equivalent electrical circuit. The results show that the CCM assembled with the Toray GDL showed the best performance at all current densities. The CCMs assembled with the Freudenberg and SGL showed similar performances up until current densities of 800 mA cm^{-2}, after which the CCM with SGL performed better. The trend in the polarisation curves can be explained using the trend in the ohmic and charge transfer resistances observed in the EIS results. If the EIS curve for Toray GDL is extrapolated at higher frequencies, the Toray GDL shows the lowest ohmic and charge transfer resistance whilst the Freudenberg GDL shows the highest.

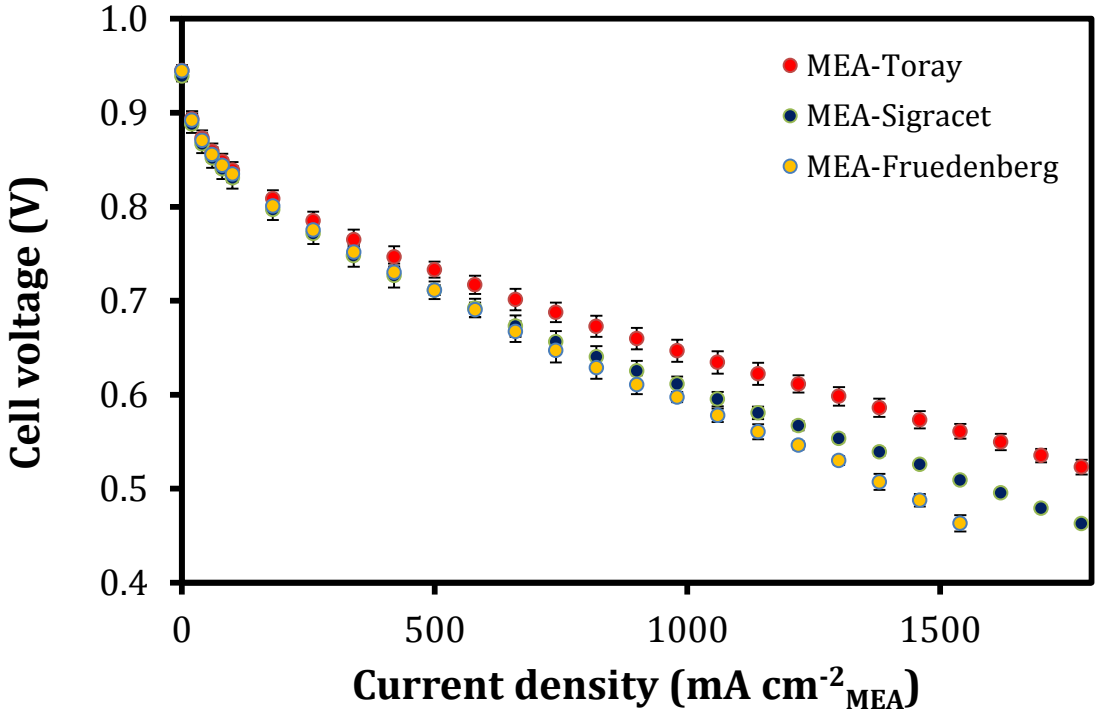

Figure 5.21: Comparison of different GDLs (T = 80 ^{0}C, P = 2 bar, $s_{hydrogen}$ = 1.5, s_{oxygen}= 10, RH_{anode} = 80% , $RH_{cathode}$ = 50%, catalyst loading = 0.4 mg Pt. cm^{-2})

A possible reason for the varying ohmic resistance may be that each commercial GDL behaves differently under the cell compression used in the test cell fixture. The compression of the cell affects both the mass transfer and the ohmic resistance. An over compression increases the mass transfer resistance and decreases the ohmic resistance, while the opposite is true for an under compression.

From Table 5.6, Toray GDL has the least through plane resistance, while Freudenberg has the highest. It is therefore unsurprising that the resistance based on the EIS was the least for the Toray GDL. A thin GDL improves the gas supply and facilitates the removal product of water, but can have a higher electronic resistance (Lee et al., 2004). From this result, the thinner GDL lead to an improved MEA performance. This further supports the theory that poor water management is inhibiting the performance of in-house MEAs. The porosity is important for similar reasons as the thickness, but without available data on the Freudenberg GDL it is difficult compare them in this case.

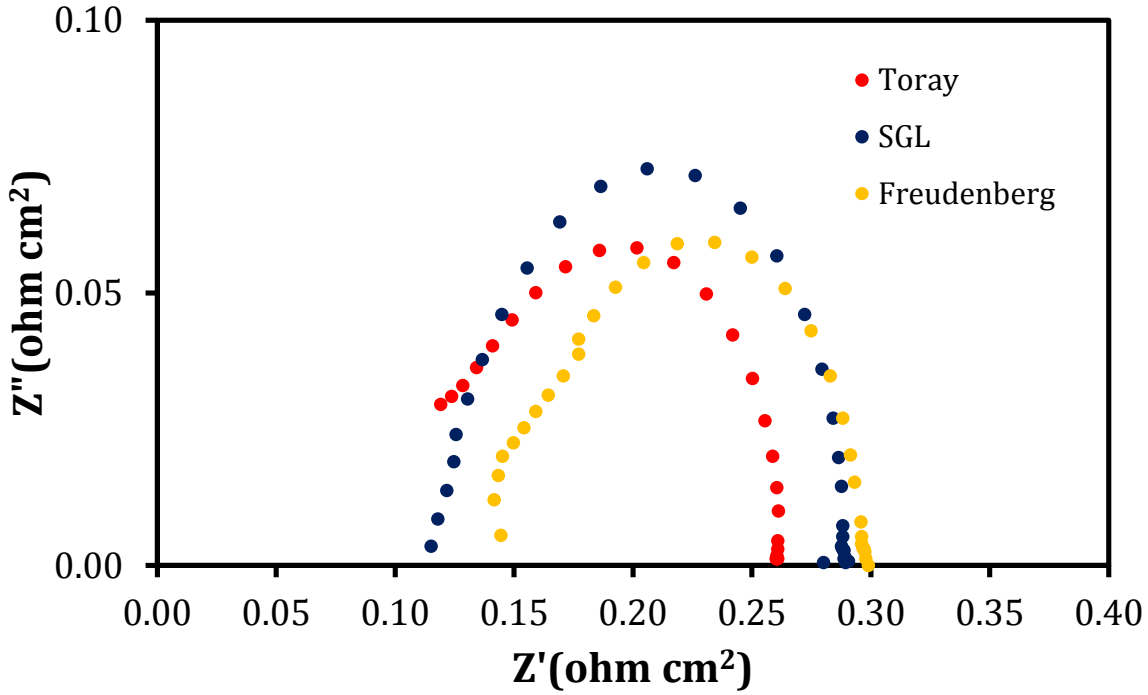

Figure 5.22: EIS comparison of different GDLs (T = 80°C, P = 2 bar, $s_{hydrogen}$ = 1.5, s_{oxygen}= 10, RH_{anode} = 80% , $RH_{cathode}$ = 50%, catalyst loading = 0.4 mg Pt/cm2, current density = 400 mA $cm^{-2}{}_{MEA}$)

Table 5.5: Equivalent circuit values for different GDLs

	Rs (ohm.cm²)	Rct (ohm.cm²)	Cdl (F)	n
Toray	0.12	0.14	0.00034	0.88
Sigracet	0.12	0.17	0.00030	0.90
Freudenberg	0.15	0.16	0.00064	0.84

Table 5.6: Commercial GDL specifications

	Through plane resistance (mΩcm²)	Thickness (µm)	Porosity (%)
Toray	5.8	190	78
Sigracet	<12	235	76
Freudenburg	15	270	

6 Concluding Remarks

Over the course of the study a newly acquired screen printer was installed and commissioned. A method of fabricating CCMs via a decal transfer was established as a platform for future developments at HySA/Catalysis.

Catalyst inks with varying amounts of isopropanol, 1,2-propanediol and water were screened for their suitability for screen printing. In particular the catalyst ink rheology required for a smooth and evenly printed surface was determined for a given screen and squeegee combination.

An ink containing 1g 40 wt% Pt/C, 2.8 ml 15 wt% ionomer solution, 0.5 ml deionised water, 3 ml 1,2-propandiol and 0.5 ml isopropanol yielded a smooth and even print as characterised by SEM and optical microscopic images. It is important to note however, that this ink was found to be suitable for a specific set of screen printing parameters such a speed of 0.6 $m.s^{-1}$ and an angle of 22°. The presence of isopropanol in the catalyst ink was found to improve fuel cell performance. This suggests that the isopropanol may be acting as a good dispersing agent leading to increased catalyst utilisation

The similarity in fuel cell performance between the in-house CCMs and two commercial CCMs suggests that the test station setup may be limiting the performance of all CCMs. Possible sources could include the flow field design and the cell compression. This is supported by the fact that for the in-house CCMs, an increase in the relative humidity from 50%/25% to 80%/50% did not cause a substantial increase in performance. This is further supported by the thinnest GDL having a superior performance

Hot pressing of GDLs onto the in-house CCMs prior to testing led to a decrease in fuel cell performance. This implies some undesirable modification to the CCM is taking place. Three different commercial GDLs were assembled with the in-house CCMs and the Toray (060T) GDL showed the best performance.

From the findings of this work, future researchers at HySA/Catalysis can further investigate and improve MEA fabrication using the established techniques of linking the rheology profile of future catalyst inks to the screen printing parameters. Furthermore, opportunities exist to improve performance on in-house MEAs by altering the water management in the cell fixture. Pathways to do this include seeking new raw materials or investigating different flow field designs.

The screen printer has shown to be a fast and reliable method of MEA fabrication, and represents an opportunity for future scale up projects.

7 References

Arico, A. et al., 2000. Influence of flow field design on the performance of a DMFC. *Journal of Power Sources*, 91, pp.202-09.

Atkins, P.W., 1998. *Physical chemistry*. 6th ed. Oxford: Oxford University Press.

Barbir, F., 2005. *PEM Fuel Cells: Theory and Practice*. 1st ed. London: Elsevier Acedemic Press.

Bender, G., Zawodzinski, T.A. & Saab, A.P., 2003. Fabrication of high precision PEFC MEA. *Journal of Power Sources*, 124, pp.114-17.

Berning, T. & Djilali, N., 2003. Three-dimensional computational analysis of transport phenomena in a PEMFC - A parametric study. *Journal of Power Sources*, 124(2), pp.440-52.

Bonifacio, R.N., Paschoal, J.O.A., Linardi, M. & Cuenca, R., 2011. Catalyst layer optimization by surface tension control during ink formulation of MEA in PEMFC. *Journal of Power Sources*, 196(10), pp.4680-85.

Chisaka, M., Matsuoka, E. & Daiguji, H., 2010. Effect of organic solvents on the pore structure of catalyst layers in PEMFCs. *Journal of the Electrochemical Society*, 157(8), pp.B1218-21.

Cooper, K., Ramani, V., Fenton, J. & Kunz, R., 2008. *Experimental methods and data analyses for PEFC*. 16th ed. North Carolina: Sribner Associates, Inc.

Debe, M.K., 2012. Effect of electrode surface area distribution on high current density performance of PEMFC. *Journal of the Electrochemical Society*, 159(1), pp.54-67.

Ferreira, P.J. et al., 2005. Instability of Pt/C electrocatalysts in PEMFCs. *Journal of the Electrochemical Society*, 152(11), pp.A2256-71.

Frey, T. & Linardi, M., 2004. Effects of MEA preparation on the PEMFC performance. *Electrochimica Acta*, 50(1), pp.99-105.

Fuller, G., 2011. *Suspension rheology*. SASOR Short Course 2011. Stanford: Stanford University.

Gasteiger, H.A., Kocha, S.S., Sompalli, B. & Wagner, F.T., 2005. Activity benchmarks and requirements for Pt, Pt-alloy, and non-Pt oxygen reduction catalyst for PEMFCs. *Applied Catalysis B: Environmental*, 56(1-2), pp.9-35.

Giacomin, A.J., 2011. *Introduction to rheology*. SASOR Short Course 2011. Madison: University of Wisconsin.

Han, M., Xu, J.H., Chan, S.H. & Jiang, S.P., 2008. Characterization of the gas diffusion layers for PEMFC. *Electrochimica Acta*, 53, pp.5361-67.

Hobson, L.J., Nakano, Y., Ozu, H. & Hayase, S., 2002. Targeting improved DMFC performance. *Journal of Power Sources*, 104(1), pp.79-84.

Hung, A.-J., Sung, L.-Y., Chen, Y.-H. & Yu, C.-C., 2007. Operation-relevant modeling of an experimental PEMFC. *Journal of Power Sources*, 171, pp.728-37.

Hwang, D.S., Park, C.H., Yi, S.C. & Lee, Y.M., 2011. Optimal catalyst layer structure of PEMFC. *International Journal of Hydrogen Energy*, 36(16), pp.9876-85.

Kimmel, T., 2012. Hydrogen and fuel cell developments in Canada. In *Hydrogen Production and Water Electrolysis*. Potchefstroom, 2012.

Kocha, S.S., 2003. Principles of MEA preparation. In W. Vielstich, A. Lamm & H.A. Gasteiger, eds. *Handbook of Fuel Cells: Volume 3 Fundamentals, Technology and Applications*. Chichester, UK: Wiley. pp.540-63.

Lee, H.-K., Park, J.-H., Kim, D.-Y. & Lee, T.-H., 2004. A study on the characteristics of the GDL thickness and porosity of the PEMFC. *Journal of Power Sources*, 131(1-2), pp.200-06.

Liao, S., Li, B. & Li, Y., 2008. Physical characterisation of electrocatalysis. In J. Zhang, ed. *PEM Fuel Cell Electrocatalysis and Catalyst Layers: Fundamentals and Applications*. 1st ed. Cape Town: Springer. pp.487-56.

Lim, J.W. et al., 2012. Ionic resistance of a cathode catalyst layer with various thickness by EIS for PEMFC. *Journal of Electrochemical Society*, 159(4), pp.378-84.

Li, H. et al., 2008. A review of water flooding issues in the PEMFC. *Journal of Power Sources*, 187(1), pp.103-17.

Mehta, V. & Cooper, J.S., 2003. Review and analysis of PEMFC design and manufacturing. *Journal of Power Sources*, 114, pp.32-53.

Millington, B., Du, S. & Pollet, B.G., 2011. The effect of materials on PEMFC electrode performance. *Journal of Power Sources*, 196(21), pp.9013-17.

Phair, J. & Kaiser, A., 2009. Determination and assessment of the rheological properties of pastes for screen printing ceramics. *Annual Transactions of the Nordic Rheology Society*, 17.

Rajalakshmi, N. & Dhathathreyan, K.S., 2007. Catalyst layer in PEMFC Electrodes - Fabrication, characterisation and analysis. *Chemical Engineering Journal*, 129, pp.31-40.

Roberts, G., 2006. *History's influence on screen printing's future*. [Online] Available at: http://www.screenweb.com/content/historys-influence-screen-printings-future [Accessed 3 July 2012].

Rodgers, M.P., Mohajeri, N., Bonville, L.J. & Slattery, D.K., 2012. Accelerated testing of PEMFCs containing Pt/C and PtCo/C Catalysts. *Journal of the Electrochemical Society*, 159(5), pp.564-69.

Sheng, A., 1999. Why ancient silk is still gold: Issues in Chinese textile history. *Ars Orientalis*, 29, pp.147-68.

Shinozaki, K., Yamada, H. & Morimoto, Y., 2011. Relative humidity dependence of Pt utilization in PEFC electrodes: Effect of thickness, ionomer to carbon ration, ionomer equivalent weight and carbon support. *Journal of Electrochemical Society*, 158(5), pp.467-75.

Song, J.M., Suzuki, S., Uchida, H. & Watanbe, M., 2006. Preparation of high catalyst utilisation electrodes for PEFC. *Langmuir*, 22(14), pp.6422-28.

Stampino, P.G. et al., 2009. Effect of different substrates, ink compositions and rheology on coating deposition of microporous layer for PEMFCs. *Catalysis Today*, 147, pp.S30-35.

Su, H.-N., Liao, S.-J., Shu, T. & Gao, H.-L., 2010. Performance of an ultra-low platinum loading MEA prepared by a novel catalyst-sprayed membrane technique. *Journal of Power Sources*, 195(3), pp.756-61.

Tang, H., Wang, S., Jiang, S.P. & Pan, M., 2007. A comparative study of CCM and hot-pressed MEAs for PEMFCs. *Journal of Power Sources*, 170(1), pp.140-44.

Tang, H., Wang, S., Pan, M. & Yaun, R., 2007. Porosity-graded micro-porous layers for PEMFCs. *Journal of Power Sources*, 166(1), pp.41-46.

Thanslip, S. & Hunsom, M., 2010. Effect of MEA fabrication techniques on the cell performance of Pt-Pd/C electrocatalyst for ORR in PEMFC. *Fuel*, 89(12), pp.3847-52.

Williams, M.V., Kunz, R.H. & Fenton, J.M., 2005. Analysis of polarization curves to evaluate polarization sources in hydrogen/air PEMFCs. *Journal of The Electrochemical Society*, 3(152), pp.A635-44.

www.mecadi.com, 2013. *Permeation & Polymers*. [Online] Available at: http://www.mecadi.com/en/literature_tools/encyclopedia/categorial/Ionomer/Nafion_copolymer_made_from_PTFE_and_perflourinate/ [Accessed 16 January 2013].

www.scientific-computing.com, 2003. *Fuel Cell Design*. [Online] Available at: http://www.scientific-computing.com/features/feature.php?feature_id=126 [Accessed 11 June 2012].

Yaun, X.-Z., Song, C., Wang, H. & Zhang, J., 2010. *Electrochemical impedance spectroscopy in PEMFCs: Fundamentals and applications*. London: Springer.

Yaun, X., Wang, H., Sun, J.C. & Zhang, J., 2007. AC impedance technique in PEMFC diagnosos - A Review. *International Journal of Hydrogen Energy*, 32(17), pp.4365-80.

8 Appendix

Reproducibility of single MEA testing					
Current	Voltage			σ_v	μ(%)
	P1	P2	P3		
0	0.94	0.94	0.94	0.00019	0.09
20	0.88	0.88	0.88	0.00019	0.09
40	0.86	0.86	0.86	0.00051	0.25
60	0.84	0.84	0.84	0.00069	0.34
80	0.83	0.83	0.83	0.00126	0.62
100	0.82	0.82	0.81	0.00139	0.68
120	0.81	0.81	0.81	0.00158	0.78
180	0.78	0.78	0.78	0.00234	1.15
240	0.76	0.76	0.75	0.00255	1.26
300	0.74	0.74	0.73	0.00233	1.15
360	0.72	0.72	0.71	0.00084	0.41
420	0.70	0.70	0.70	0.00051	0.25
480	0.68	0.68	0.68	0.00058	0.28
540	0.66	0.66	0.66	0.00038	0.19
600	0.65	0.65	0.65	0.00084	0.41
660	0.63	0.63	0.63	0.00153	0.75
720	0.61	0.62	0.61	0.00158	0.78
780	0.60	0.60	0.60	0.00231	1.14
840	0.58	0.59	0.58	0.00315	1.55
900	0.57	0.58	0.57	0.00342	1.69
960	0.56	0.56	0.56	0.00203	1.00
1020	0.54	0.55	0.54	0.00473	2.33
1080	0.53	0.53	0.52	0.00668	3.29
1140	0.51	0.51	0.51	0.00416	2.05
1200	0.50	0.50	0.49	0.00495	2.44

Example of raw data workup for EIS (Commercial CCM)			
Real		Imaginary	
m ohm	ohm cm2	m ohm	ohm cm2
5.97	0.149	-0.13	0.003
6.09	0.152	-0.24	0.006
6.23	0.156	-0.37	0.009
6.37	0.159	-0.49	0.012
6.81	0.170	-0.65	0.016
7.22	0.181	-0.83	0.021
7.53	0.188	-1.03	0.026
7.73	0.193	-1.25	0.031
7.95	0.199	-1.52	0.038
8.26	0.207	-1.86	0.047
8.59	0.215	-2.29	0.057
9.00	0.225	-2.81	0.070
9.55	0.239	-3.44	0.086
10.27	0.257	-4.17	0.104
11.21	0.280	-4.99	0.125
12.4	0.310	-5.82	0.146
13.78	0.345	-6.56	0.164
15.67	0.392	-7.13	0.178
17.52	0.438	-7.3	0.183
19.48	0.487	-7.09	0.177
25.32	0.633	-1.77	0.044
25.48	0.637	-1.46	0.037
25.86	0.647	-1.2	0.030
26.17	0.654	-0.8	0.020
26.29	0.657	-0.53	0.013
26.3	0.658	-0.34	0.009
26.47	0.662	-0.28	0.007
26.37	0.659	-0.1	0.003
26.33	0.658	0.12	-0.003
26.23	0.656	0.25	-0.006
26.3	0.658	-0.34	0.009
26.47	0.662	-0.28	0.007
26.37	0.659	-0.1	0.003
26.33	0.658	0.12	-0.003
26.23	0.656	0.25	-0.006

Equivalent circuit values with error %								
	Rs	Rs error (%)	Rct	Rct error (%)	Cdl	Cdl error (%)	n	n error (%)
Commercial CCM (Ion Power)	0.20	2.23	0.61	2.30	0.00082	2.11	0.72	2.50
In-house CCM	0.17	1.36	0.50	1.68	0.00129	2.23	0.77	0.63
CCM with hot press	0.15	1.09	0.21	0.86	0.00031	1.02	0.86	0.36
CCM without hot press	0.15	1.75	0.16	2.42	0.00064	3.91	0.84	1.02
Toray	0.12	1.05	0.14	0.97	0.00034	1.05	0.88	0.38
SGL	0.12	0.44	0.17	0.51	0.00030	0.86	0.90	0.18
Freudenberg	0.15	1.75	0.16	2.42	0.00064	3.91	0.84	1.02